SANDIA REPORT

SAND 2003-3784
Unlimited Release
Printed October 2003

Equations of State for Be, Ni, W, and AU.

Author(s)Gerald I. Kerley

Prepared by
Sandia National Laboratories
Albuquerque, New Mexico 87185 and Livermore, California 94550

Sandia is a multiprogram laboratory operated by Sandia Corporation,
a Lockheed Martin Company, for the United States Department of Energy's
National Nuclear Security Administration under Contract DE-AC04-94AL85000.

Issued by Sandia National Laboratories, operated for the United States Department of Energy by Sandia Corporation.

Available to DOE and DOE contractors from
U.S. Department of Energy
Office of Scientific and Technical Information
P.O. Box 62
Oak Ridge, TN 37831

Telephone: (865)576-8401
Facsimile: (865)576-5728
E-Mail: reports@adonis.osti.gov
Online ordering: http://www.doe.gov/bridge

Available to the public from
U.S. Department of Commerce
National Technical Information Service
5285 Port Royal Rd
Springfield, VA 22161

Telephone: (800)553-6847
Facsimile: (703)605-6900
E-Mail: orders@ntis.fedworld.gov
Online order: http://www.ntis.gov/help/ordermethods.asp?loc=7-4-0#online

SAND2003-3784
Unlimited Release
Printed October 2003

Equations of State for Be, Ni, W, and Au

Gerald I. Kerley, Consultant
Kerley Technical Services
P.O. Box 709
Appomattox, VA 24522-0709

Abstract

The PANDA code is used to construct tabular equations of state (EOS) for four metals— beryllium, nickel, tungsten and gold. Each EOS includes melting, vaporization, and thermal electronic excitation. Separate EOS tables are constructed for the solid and fluid phases, and the PANDA phase transition model is used to construct a multiphase EOS table for each metal. These new EOS tables are available for use with the CTH code and other hydrocodes that access the CTH database.

Acknowledgements

Sandia is a multiprogram laboratory operated by Sandia Corporation, a Lockheed Martin Company, for the United States Department of Energy's National Nuclear Security Administration under Contract DE-AC04-94AL85000. I am grateful to Sandia for supporting this work. I especially appreciate the efforts of Gene Hertel in the production of this report.

Contents

Figures

Tables

Symbols and Units

ρ	density [g/cm^3]
V	specific volume, $V = 1/\rho$ [cm^3/g]
T	temperature [K]
P	pressure [GPa]
E	specific internal energy [MJ/kg]
A	Helmholtz free energy [MJ/kg]
S	entropy [$MJ/(kg\text{-}K)$]
β	isothermal bulk modulus, $\beta = \rho(\partial P/\partial\rho)_T$ [GPa]
C_S	sound velocity [km/s]
U_S	shock velocity [km/s]
u_P	particle velocity [km/s]
R	gas constant [8.31451×10^{-3} $MJ/kg\text{-}mole\text{-}K$]
W	atomic or molecular weight [$g/mole$]
k	Boltzmann's constant [1.38066×10^{-29} MJ/K]

1. Introduction

Sandia National Laboratories (SNL) maintains an equation of state (EOS) database for use with the three-dimensional hydrodynamics code CTH [1]-[3]. This database includes default parameters for a number of materials and for several EOS models that are described in Refs. [4][5]. The present study is part of a continuing effort to evaluate and improve this database [6][7].

A recent evaluation of the database revealed that many of the tabular EOS for metals had serious deficiencies [7][8]. The present report discusses new EOS tables for four important metals that fall in that category—beryllium (Be), nickel (Ni), tungsten (W), and gold (Au). These metals were selected for study, not because they have similar properties, but because the same basic approach could be used for all of them.

The new EOS tables were constructed using the PANDA code [9]. The model used here, which is similar to that previously used for aluminum [10], is discussed in Sec. 2. It includes melting, vaporization, and thermal electronic excitation, but not polymorphic phase transitions. Be and Ni both have more than one solid phase, but the solid-solid transitions do not appear to affect the EOS enough to justify including them in the model.[1]

Sections 3-6 of this report discuss each of the metals—beryllium in Sec. 3, nickel in Sec. 4, tungsten in Sec. 5, and gold in Sec. 6. The model predictions are compared with thermophysical, sound speed, melting, static compression, and shock Hugoniot data.

As in previous work, the thermal electronic contributions to the EOS are computed by merging calculations from two quantum-statistical theories. This part of the model involves several new features and requires a rather lengthy discussion, which is given in Appendix A.

Conclusions are summarized in Sec. 7.

Appendix B shows plots of the tension region for the four materials.

1. A multiphase model for titanium that includes solid-solid transitions, similar to that previously used for iron [11], is being developed separately and will be discussed in another report [12].

2. Overview of EOS Model

The EOS tables were constructed with the PANDA code [9], using a model similar to that previously applied to aluminum [10]. Separate EOS tables were constructed for the solid and fluid phases, and the phase transition option was used to construct a single table including melting and vaporization.

2.1 Solid Phase

The thermodynamic functions for the solid phase were expressed as sums of terms that are assumed to be separable and additive:

$$P(\rho, T) = P_c(\rho) + P_l(\rho, T) + P_e(\rho, T), \tag{1}$$

$$E(\rho, T) = E_c(\rho) + E_l(\rho, T) + E_e(\rho, T) - \Delta E_b \tag{2}$$

$$A(\rho, T) = E_c(\rho) + A_l(\rho, T) + A_e(\rho, T) - \Delta E_b . \tag{3}$$

The subscripts c, l, and e denote contributions from the zero-Kelvin curve, lattice vibrations, and thermal electronic excitations, respectively. The constant ΔE_b was chosen to give zero energy at room temperature and pressure (RTP). A magnetic term was also included in the EOS for nickel (Sec. 4).

The zero-Kelvin curves were fit to the Birch-Murnaghan equation [13],

$$P_c(\rho) = \frac{3}{2}\beta_0(\eta^{7/3} - \eta^{5/3})\left[1 + \frac{3}{4}(\eta^{2/3} - 1)(\beta'_0 - 4)\right], \tag{4}$$

$$E_c(\rho) = \frac{9\beta_0}{8\rho_0}(\eta^{2/3} - 1)^2\left[\frac{1}{2}(\eta^{2/3} - 1)(\beta'_0 - 4) + 1\right], \tag{5}$$

where $\eta = \rho/\rho_0$, and ρ_0, β_0, and β'_0 are constants. These constants were determined by fitting the model to the RTP density and sound speed, Hugoniot and static compression data, and band-theoretical calculations, where available. To ensure correct asymptotic behavior at high densities, the PANDA extrapolation formula, which is based on Thomas-Fermi-Dirac (TFD) theory, was used at pressures above about 200 GPa (match density RTFD).

The lattice-vibrational terms were computed using the well-known Debye model; the equations are given in Sec. 4.2 of the PANDA manual. The model requires two input constants, GREF and DEBREF, the Grüneisen parameter and Debye temperature at the RTP density ρ_{ref}. These two parameters were determined by fitting thermal expansion and heat capacity data [14]-[16]. The density dependence of

the Grüneisen function was computed from the generalized Dugdale-MacDonald formula, discussed in Sec. 4.5 of the PANDA manual.

The thermal electronic terms (which are also included in the fluid EOS) were constructed by merging calculations from two theories—the PANDA ionization equilibrium (IEQ) model at low densities, and a modified version of Liberman's INFERNO model [17] at high densities. The details of these calculations are somewhat complicated and are discussed in the appendix.

The seven parameters for the solid models of Be, Ni, W, and Au are given in Table 1 and discussed in Secs. 3-6.

2.2 Fluid Phase

The thermodynamic functions for the fluid phase—which includes the liquid, gas, and supercritical regions—were calculated using the PANDA liquid model. The Helmholtz free energy has the form

$$A(\rho, T) = A_\phi(\rho, T) + A_e(\rho, T) - T \ln w_{liq} - \Delta E_b. \quad (6)$$

Here A_ϕ includes the contributions from both the intermolecular forces and the thermal motions of the molecular centers of mass, and A_e is the contribution from thermal electronic excitations, the same as in the solid phase. w_{liq} is a constant that is used to match the entropy of the liquid at the melting point. The constant ΔE_b is the same as for the solid phase (except for nickel). The other thermodynamic quantities were computed from the usual thermodynamic relations.

The first term in Eq. (6), A_ϕ, was calculated using a version of liquid perturbation theory called the CRIS model [18][19]. This model has been discussed in detail in previous work, and we will review only a few points here.

The thermodynamic properties of a fluid are determined by the potential energy ϕ of a molecule in the field of neighboring molecules. The free energy A_ϕ can be written in terms of this function by using a perturbation expansion about the properties of an idealized hard-sphere fluid,

$$A_\phi(\rho, T) = A_0(\rho, T, \sigma) + (N_0/W)\langle\phi\rangle_0 + \Delta A, \quad (7)$$

where N_0 is Avogadro's number and W is the molecular weight. Here A_0 is the free energy for a fluid of hard spheres, the first-order term $\langle\phi\rangle_0$ is an average of ϕ over all configurations of the hard sphere fluid, and ΔA includes all higher-order terms in the expansion. The hard-sphere diameter σ is defined by a variational principle that minimizes $|\Delta A|$, which selects the hard-sphere system having a

structure that is closest to that of the real fluid. The corrections ΔA are then computed from approximate expressions.

It is not currently possible to determine the function ϕ, which depends upon the intermolecular forces, from either experiment or theory. In the CRIS model, this function is estimated from the zero-Kelvin energy of the solid phase by

$$\phi \approx (\rho / \rho_s) E_c(\rho_s) \ , \tag{8}$$

where ρ is the actual density of the fluid, and ρ_s is the solid density having the same nearest neighbor distance as that of the given fluid configuration. Equation (8) is then averaged over all nearest neighbor distances using equations derived from the hard-sphere distribution function [18][19]. This approximation has been found to give good results for many kinds of liquids, including liquid metals.

Hence the CRIS model allows one to compute the EOS properties of the fluid phase from the zero-Kelvin isotherm already determined for the solid phase. However, there are two additional considerations.

- The zero-Kelvin curve is extended into tension using the so-called LJ MATCH option, requiring three parameters—ECOH, RLJ, and FACLJ.
- PANDA also uses two parameters—w_{liq} and EFAC—for "tuning" the model to match the enthalpy and entropy at the melting point.

These five additional parameters are discussed in Secs. 2.4 and 5 of the PANDA manual. The values used in this work are given in Table 1. The most important parameter, the cohesive energy of the solid at 0K (ECOH), was computed from data in Refs. [15], [16], and [20].

2.3 Multiphase EOS Table

The PANDA phase transition model (MOD TRN option) was used to compute the melting curve and construct the final EOS for each metal. The density range of the table went from 0 to a maximum corresponding to a pressure of 10 TPa (at 0K). The temperature range was $0 \le T \le 1.0 \times 10^8$ K. The mesh points were chosen to give good resolution of the important features of the EOS surface. In order to allow treatment of fracture models, a tension region was included at temperatures below the boiling point, while Maxwell constructions were included at all higher temperatures.

Table 1: Parameters for EOS models.

parameter	Be	Ni	W	Au
ρ_{ref} (g/cc)	1.8452	8.9092	19.255	19.288
ρ_0 (g/cc)	1.8882	9.0191	19.347	19.528
β_0 (GPa)	120.0	189.0	310.0	181.0
β'_0	3.41	4.70	3.79	5.50
RTFD	2.5	15.0	25.0	35.0
GREF	1.189	1.850	1.723	2.850
DEBREF (K)	960.0	375.0	340.0	185.0
ECOH (MJ/kg)	35.48	7.286	4.613	1.858
RLJ (g/cc)	1.65	8.0	17.5	17.5
FACLJ	1.0	1.0	1.0	2.0
EFAC (MJ/kg)	0.286	0.266	0.157	0.0884
w_{liq}	1.0	3.77	1.0	3.30

3. Beryllium

The present work is a refinement of earlier calculations reported in [21] and [22], the biggest change being in the thermal electronic term.

Be has two solid phases at zero pressure [23][24]. The stable phase at low temperature is hcp, and a transition to bcc occurs just before melting. It has been suggested that the bcc phase would become more stable under pressure, giving rise to a phase transition at about 8 GPa on the Hugoniot. However, Hugoniot and wave profile measurements do not show any effects of the transition on shock wave propagation [25][26]. Static measurements show a transition from hcp to a distorted hcp phase in the pressure range 8.6-14.5 GPa, but the volume change of the transition is very small [27]. X-ray diffraction studies of Be shocked to 22.8 GPa show only the hexagonal phase [28]. Melting occurs at 1560K at zero pressure.

Because definitive data about the phase transitions in Be are not yet available, we have modeled the solid as a single phase in this study. The solid parameters, given in Table 1, were fit to the following experimental data: density [14][20], enthalpy and entropy [15][16], ultrasonic [29][30], Hugoniot data up to 90 GPa [25][31], and band-theoretical calculations at high pressures [32][33]. For the liquid, the tension region of the cold curve was chosen to match the experimental binding energy, and the parameter EFAC was chosen to match the enthalpy at the melting point. No entropy correction was needed, so $w_{liq} = 1$.

The model results are compared to zero-pressure thermophysical data in Fig. 1. For completeness, we also show the isobaric expansion data of Boivineau, et al. [34], although their results cannot be considered credible, especially in the case of the density. (They admitted to having problems, the measurements not being reproducible from shot to shot.) The model agrees well with the other data.

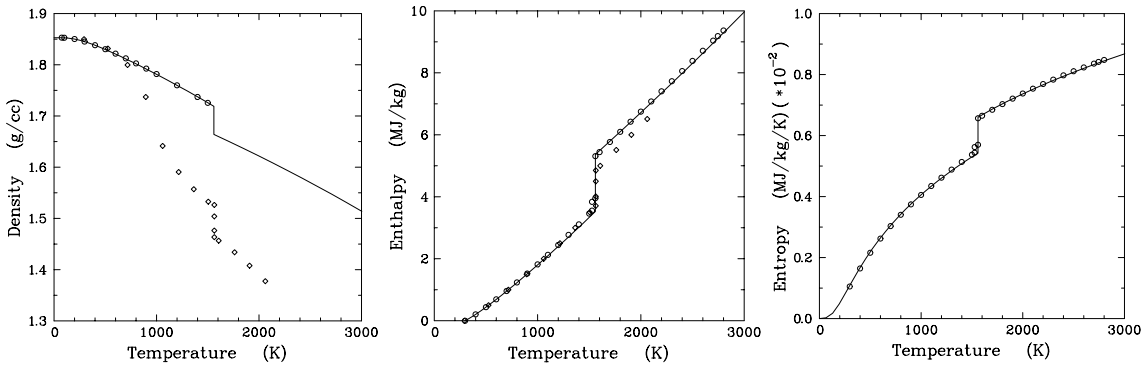

Fig. 1. Comparison of model with thermophysical data for Be. Density: circles—solid at P=0 [14], diamonds—isobaric data at .12 GPa [34]. Enthalpy and entropy: circles—solid and liquid at P=0 [15], diamonds—isobaric data at .12 GPa [34]. Solid lines are from model.

The beryllium Hugoniot is shown in Fig. 2. The left side of the figure compares the calculated curve with experimental data up to about 200 GPa [25][31][35]. The dashed portion of the calculated curve corresponds to the melting region, 4.6-5.9 km/s. Steinberg's model and parameters were used to compute strength corrections to the solid Hugoniot [36]. The strength terms are not negligible; for comparison, the Hugoniot computed without strength is shown by a dotted line. The model also agrees well with three sets of data in the ultra-high pressure region, shown on the right side of Fig. 2.[1] The model predicts a drop in shock velocity on melting but a 10% *increase* in the slope of the Hugoniot in the liquid region, in agreement with the experimental data.

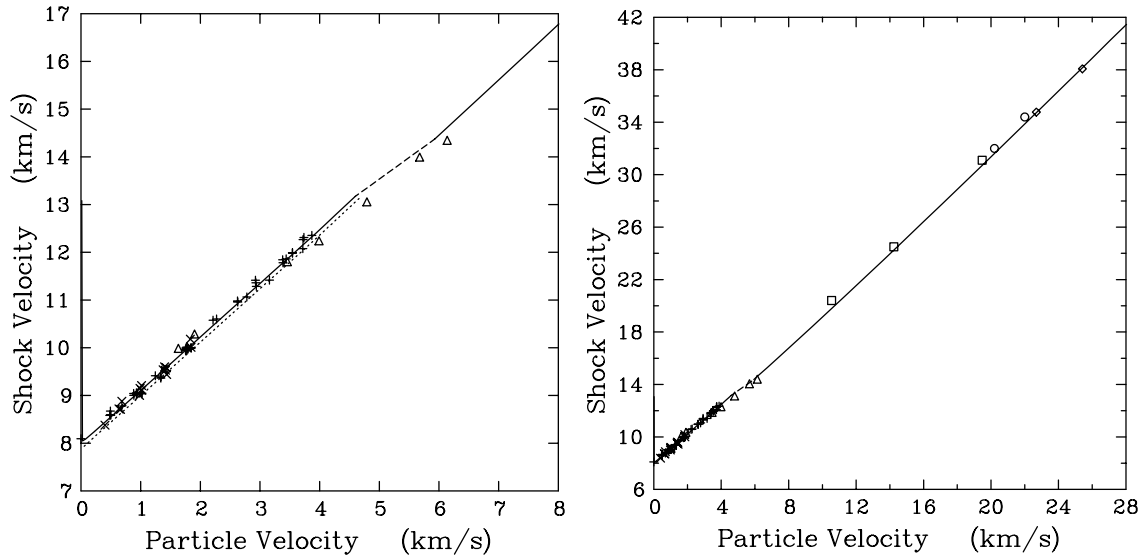

Fig. 2. Beryllium Hugoniot in shock velocity-particle velocity plane. Curves were computed from model; dashed region shows melting region, and dotted curve shows calculations for solid without material strength. Left side gives data up to about 200 GPa, shown by x's [25], crosses [31], and triangles [35]. Right side includes ultra-high shock data up to 2 TPa, shown by diamonds [37], squares [38], and circles [39].

The predicted melting curve and Hugoniot are shown in Fig. 3. The model predicts shock melting to begin at 112 GPa and be complete at 157 GPa. It is interesting to note that the model predicts shock melting in beryllium to occur at an anomalously low pressure, compared to other metals. For example, our model predicts shock melting to occur at 186 GPa in copper [41] and 212 GPa in gold (Sec. 6), even though those metals have *lower* melting temperatures at zero pres-

1. The three Hugoniot points of Nellis, et al., were made relative to an aluminum standard [38]. Knudson has recently reported accurate measurements of the aluminum Hugoniot in this pressure regime [40]. His results differ significantly from the EOS that was used to analyze the data in [38]. The data shown by squares in Fig. 2 have been corrected for the change in the standard. The correction increases the particle velocities by about 2%.

sure. Our value for beryllium is close to that for aluminum [10], which has a much lower melting point at zero pressure (933K). The principal reason for this fact is that the predicted melting curve for beryllium depends only weakly on temperature, as seen in Fig. 3.

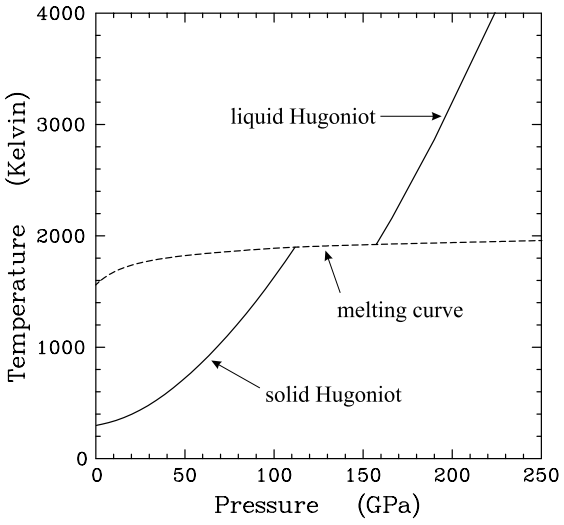

Fig. 3. Calculated melting curve and Hugoniot for Be.

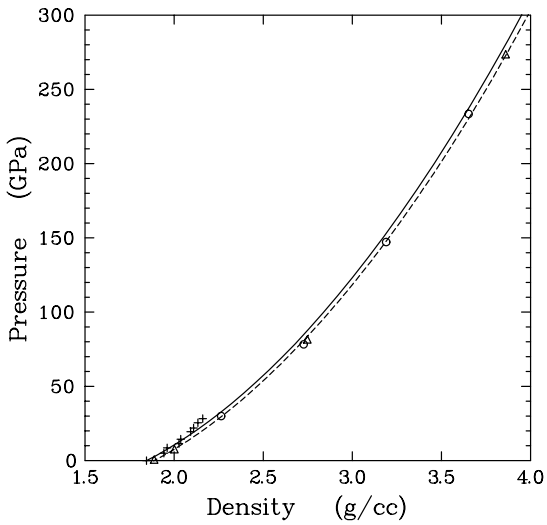

Fig. 4. Static compression curves for Be. Crosses [27], circles [32], and triangles [33]. Calculated RT curve is shown by a solid line, 0K curve by a dashed line.

The onset of shock melting can be inferred experimentally, by measuring the sound speed behind the shock front. Such measurements typically yield longitudinal wave speeds, higher than bulk sound speeds, in the solid region. A transition to the bulk sound speed at high pressures is taken as evidence of melting. Unfortunately, measurements of this type are not available for beryllium. However, the fact that our model shows a change in slope of the Hugoniot, in agreement with the data, is evidence that our shock melting prediction is reasonable.

Figure 4 compares the predicted room temperature and zero-Kelvin isotherms for beryllium with the static measurements of Ming and Manghnani [27] and the band-theoretical calculations of Perrot [32] and Liberman [33]. The two sets of calculated points shown in Fig. 4 have been shifted in density to match the value at zero pressure, bringing them into good agreement with one another and with our zero-Kelvin curve. Our zero-pressure curve is also in good agreement with the band-theoretical calculations of McMahan [42] (with a density shift), but his data are not shown in Fig. 4 since they have not yet been published.

In constructing the EOS table, special attention was given to the treatment of tension and vaporization. Maxwell constructions were included at temperatures above the boiling point, so that the EOS describes equilibrium vaporization at

high temperatures. A nonequilibrium tensile region was left at temperatures below the boiling point, so that the EOS will give a correct prediction of spallation in hydrodynamic code calculations.

The behavior of the EOS in the vapor-liquid region is shown in Fig. 5. The pressure is plotted as a function of density on 25 isotherms from 3000K to 20,000K. The predicted critical point is at 13,000K, 0.7 GPa, and 0.12 g/cc. The liquid density on the coexistence curve shows significant expansion at temperatures above about 6000K. This behavior is due to the effect of the metal-insulator transition on the thermal electronic contributions to the EOS.

The EOS table for beryllium covers the density range from 0.0 to 200 g/cc and the temperature range from 5 to 1.0×10^8 K. It has been given material number 2010.

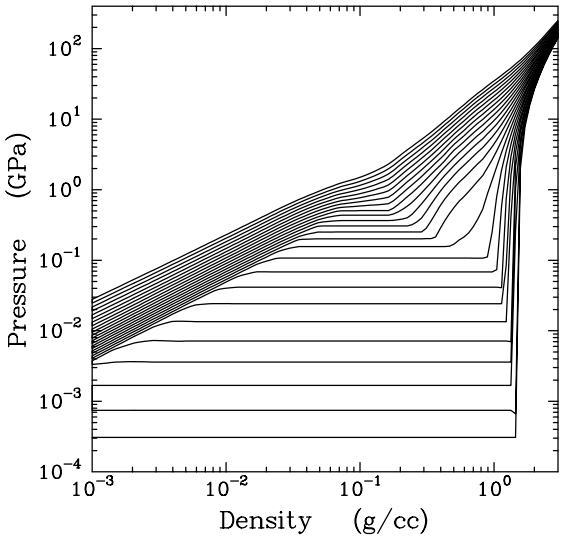

Fig. 5. EOS of beryllium in vapor-liquid transition region. There are 25 isotherms at temperatures from 3000K to 20,000K, equally spaced in the logarithm.

4. Nickel

Nickel has the fcc structure at RTP [23][24]. No other solid phases have been reported, either at high temperatures or high pressures. However, solid Ni is ferromagnetic and has a Curie temperature of 631K [15][20]. Melting occurs at 1728K at zero pressure.

The solid parameters, given in Table 1, were fit to the following experimental data: density [14][20], enthalpy and entropy [15], ultrasonic [31], static data [43], Hugoniot [31][35][44]-[46], and band theoretical calculations [47]. A satisfactory fit to the enthalpy and entropy could not be obtained without including a magnetic term. We have used Andrews' expression for the magnetic contribution to the heat capacity of alpha-phase iron [48], written in the following form.

$$C_{VM} = K_A T^{3/2}/(r_A T_C - T),\ T < T_C, \tag{9}$$

$$C_{VM} = K_B/(T - r_B T_C)^2,\ T > T_C, \tag{10}$$

where T_C is the Curie temperature, and K_A, K_B, r_A, and r_B are constants. The constants K_A and K_B, along with the Debye temperature (DEBREF in Table 1), were adjusted to fit the enthalpy and entropy, while Andrews' values for r_A and r_B were left unchanged. The result was: $K_A = 1.98 \times 10^{-6}$, $K_B = 1.31$, $r_A = 1.089$, $r_B = 0.816$ (C_{VM} in MJ/kg/K). These expressions were integrated to give the magnetic contributions to the energy and entropy; the magnetic contribution to the pressure was assumed to be zero.

For the liquid, the tension region of the cold curve was chosen to match the experimental binding energy, and the parameters EFAC and w_{liq} were chosen to match the enthalpy and entropy at the melting point. A rather large value of w_{liq} was needed because of the magnetic term. The value of ΔE_b for the liquid phase [Eq. (6)] was taken to be that for the solid phase plus the magnetic energy at the melting point.

The model results are compared to zero-pressure thermophysical data and isobaric expansion measurements in Fig. 6. The agreement is satisfactory. Hixson, et al. have measured the sound speed of liquid nickel at 0.2 GPa from the melting point up to 3200K [50]. The predicted sound speeds (not shown in Fig. 6) are within 3% of those data.

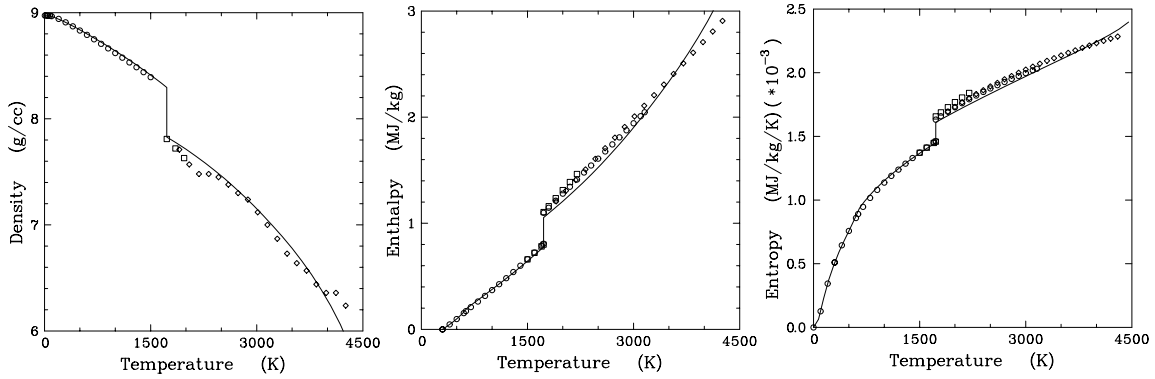

Fig. 6. Comparison of model with thermophysical data for Ni. Density: circles—solid at P=0 [14][20], squares—liquid at P=0 [20], diamonds—liquid at 0.2 GPa [50]. Enthalpy and entropy: circles—solid and liquid at P=0 [15], squares—solid and liquid at P=0 [49], diamonds—liquid at 0.2 GPa [50]. Solid lines are from model.

The nickel Hugoniot is shown in Fig. 7. The left side of the figure compares the calculated curve with experimental data [31][35][44]-[46] up to 500 GPa. The dashed portion of the curve corresponds to the melting region, 3.32-4.03 km/s. Strength terms were included in computing the Hugoniot in the solid region but have only a small effect on the results. The right side extends the comparison up to a pressure of 1.1 TPa.

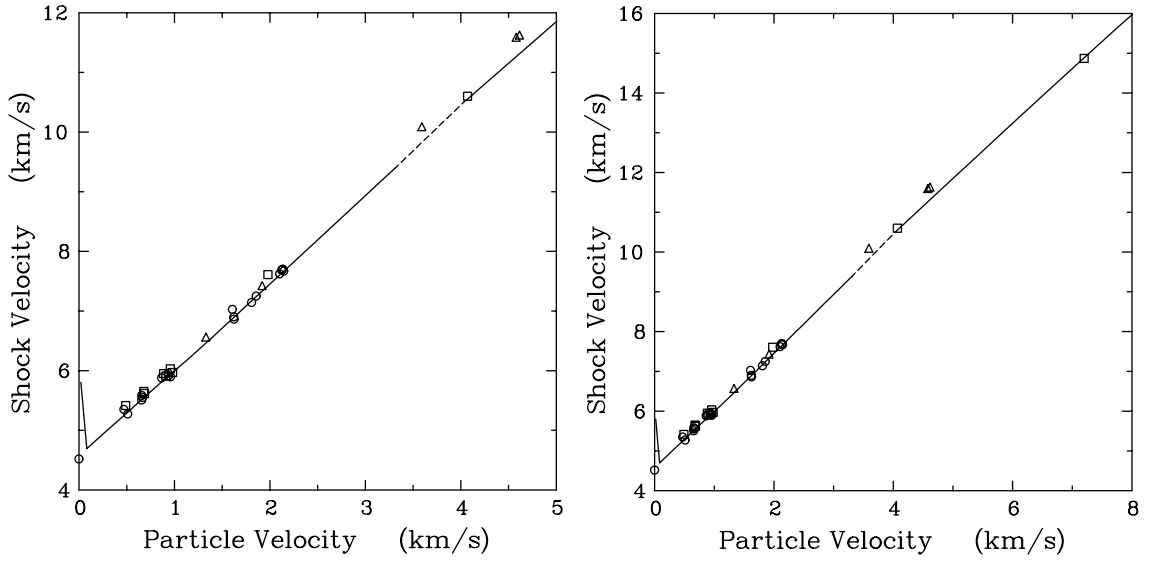

Fig. 7. Nickel Hugoniot in shock velocity-particle velocity plane. Curves were computed from model; dashed region shows melting region. Left side gives data up to 500 GPa, shown by circles [31], squares [44]-[46], and triangles [35]. Right side gives data up to 1 TPa.

The predicted Hugoniot agrees well with existing data up to 160 GPa. The two sets of data at higher pressures [35][45] are not in good agreement with one another. Our model agrees well with the data of Ref. [45]. Agreement with the data of Ref. [35] could be improved by adjusting the cold curve at high pressures, but that would worsen agreement with band-theoretical calculations [47], shown below. New shock measurements in the high pressure region would be useful.

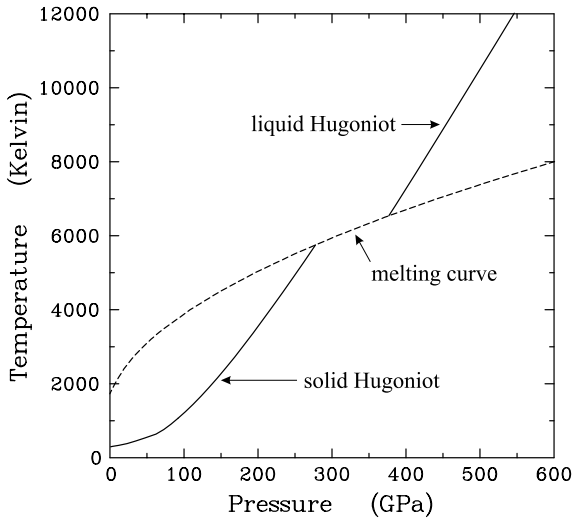

Fig. 8. Calculated melting curve and Hugoniot for Ni.

The predicted melting curve and Hugoniot are shown in Fig. 8. The model predicts shock melting to begin at 278 GPa and be complete at 377 GPa. As in the case of beryllium, there are no sound speed measurements or other data to test the prediction. Neither the model nor the experimental data indicate a significant change in slope of the Hugoniot at melting. Here again, new measurements would be useful. The model is within 2% of the measured melting temperature at 6 GPa [23].

Figure 9 compares the predicted room temperature and zero-Kelvin isotherms for nickel with the static measurements [43] and band-theoretical calculations [47]. (The calculations were shifted in density to match the density at zero pressure.) A stiffer zero-Kelvin isotherm, which would be required to match the shock data of Ref. [35], would give poorer agreement with the band-theoretical calculations but might still be within the theoretical uncertainties. Static measurements at higher pressures, along with more extensive theoretical electronic structure calculations, would be useful.

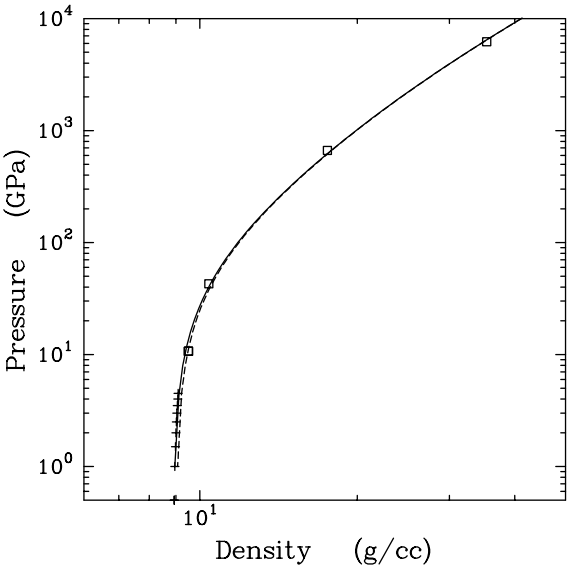

Fig. 9. Room temperature and 0K curves for nickel. Crosses [43], squares [47].

In constructing the EOS table, Maxwell constructions were included at temperatures above the boiling point, and a tensile region was left at low temperatures for the treatment of spall states. The table covers the density range from 0 to 200 g/cc

and the temperature range from 5 to 1.0×10^8 K. It has been given material number 3110.

The behavior of the EOS in the vapor-liquid region is shown in Fig. 10. The pressure is plotted as a function of density on 25 isotherms from 3000K to 15,000K. The EOS exhibits a "plasma phase transition" (PPT) in the temperature range 4525-4800K and densities in the range 4.35-5.35 g/cc. This feature, also seen in our models for aluminum [10] and copper [41], arises from the effect of the metal-insulator transition on the thermal electronic contribution to the EOS, as discussed in Appendix A. At temperatures below 4525K, there is a single coexistence region between the vapor and the metallic liquid. At higher temperatures, there are two coexistence regions, one between the vapor and an insulating liquid, the other between the insulating and metallic liquids. The critical point for the vapor-insulator region occurs at 6000K, 0.29 GPa, and 1.34 g/cc; this temperature is lower than that obtained by other theorists [51], presumably because of our treatment of the thermal electronic term.

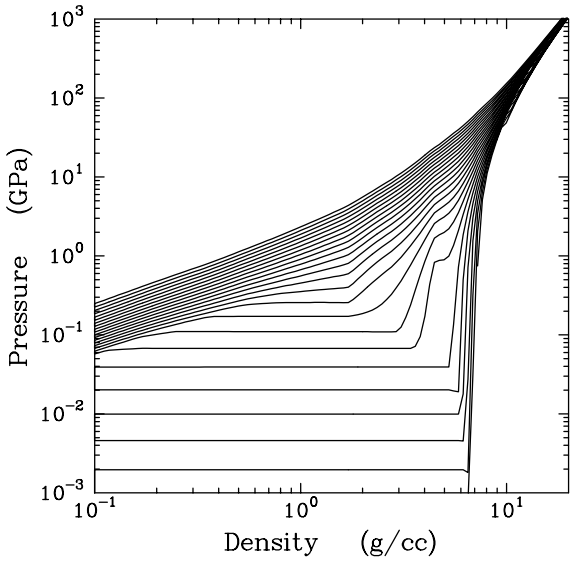

Fig. 10. EOS of nickel in vapor-liquid transition region. There are 25 isotherms at temperatures from 3000K to 15,000K, equally spaced in the logarithm.

There is no evidence for the existence of a PPT as yet, and this region of the EOS surface requires further study. Ternovoi, et al., have observed anomalous expansion velocities of shocked porous nickel at release pressures below 0.1 GPa [52]. According to our model, the release curve in their experiment passes through the region of the PPT. However, our model does not predict the large velocities that were observed. The anomalous expansion may be connected with heterogeneous heating of the highly porous samples, i.e., the formation of hot spots due to pore collapse by the shock. It is not clear whether or not a PPT would contribute to the behavior.

Gudarenko, et al., used the impedance matching technique to obtain pressure-particle velocity points on the release isentropes of porous nickel shocked to two different pressures [53]. The initial density of the samples was 3.85 g/cc. Release isentropes were measured for shock states of 60 and 100 GPa. Our calculations are compared with their data in Fig. 11. The predictions are similar to those obtained with their "EOS 2," shown in Fig. 2 of their paper. Agreement with the data is especially good for the 60 GPa shock state. The results for the 100 GPa shock state,

which we predict to pass through the region of the PPT, is not as good. It is not clear what is responsible for this discrepancy, which is also seen in their own model predictions. Here again, further study of this region would be useful.

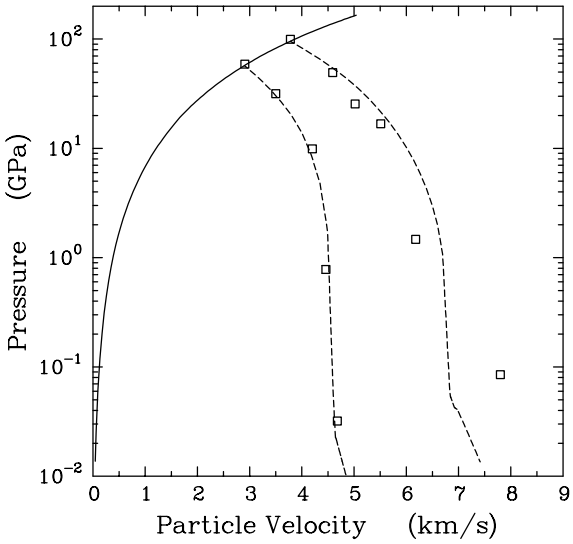

Fig. 11. Expansion isentropes of porous nickel (initial density 3.85 g/cc). Hugoniot is shown by a solid line, isentropes by dashed lines. Squares are data from [53].

5. Tungsten

Tungsten has the bcc structure at RTP [23][24]. No other solid phases have been reported, either at high temperatures or high pressures. Melting occurs at 3695K at zero pressure.

It should be noted that tungsten is usually alloyed with other elements (Ni, Cu, Fe) for use in engineering materials. The model discussed here is for pure tungsten. See the comments at the end of this section for recommendations concerning the treatment of tungsten alloys.

The solid parameters, given in Table 1, were fit to the following experimental data: density [14][20], enthalpy and entropy [15], ultrasonic [54][55], static compression [56][57], and Hugoniot [31][58]. For the liquid, the tension region of the cold curve was chosen to match the experimental binding energy, and the parameter EFAC was chosen to match the enthalpy at the melting point. No entropy correction was needed, so $w_{liq} = 1$.

The model results are compared to zero-pressure thermophysical data and isobaric expansion measurements in Fig. 12.

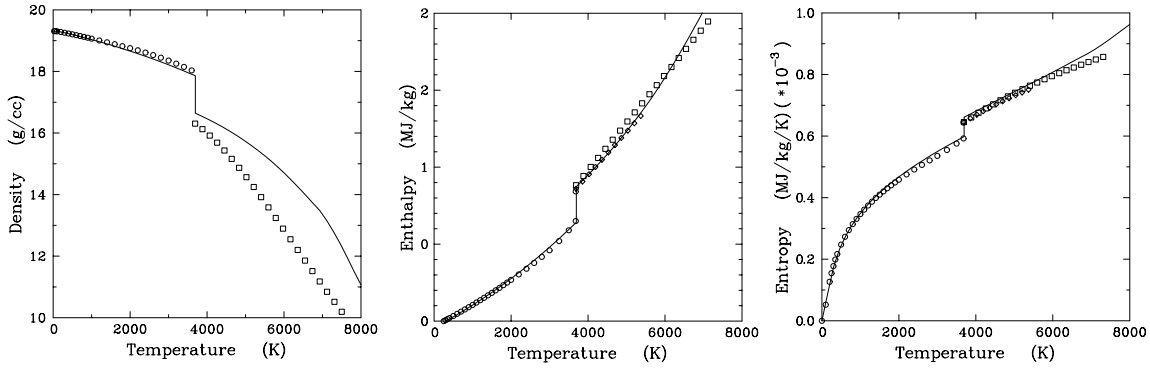

Fig. 12. Comparison of model with thermophysical data for W. Density: circles—solid at P=0 [14][20], squares—liquid isobar [59]. Enthalpy and entropy: circles—solid at P=0 [15], squares and diamonds—liquid isobars [59]. Solid lines are from model.

The tungsten Hugoniot is shown in Fig. 13. The left side of the figure compares the calculated curve with experimental data [31][58] up to about 900 GPa. The dashed portion of the curve corresponds to the melting region, 2.63-3.18 km/s. Strength terms were included in computing the Hugoniot in the solid region; for comparison, the Hugoniot computed without strength is shown by a dotted line. The right side of Fig. 13 includes one ultra-high pressure point at 6.5 TPa [37].

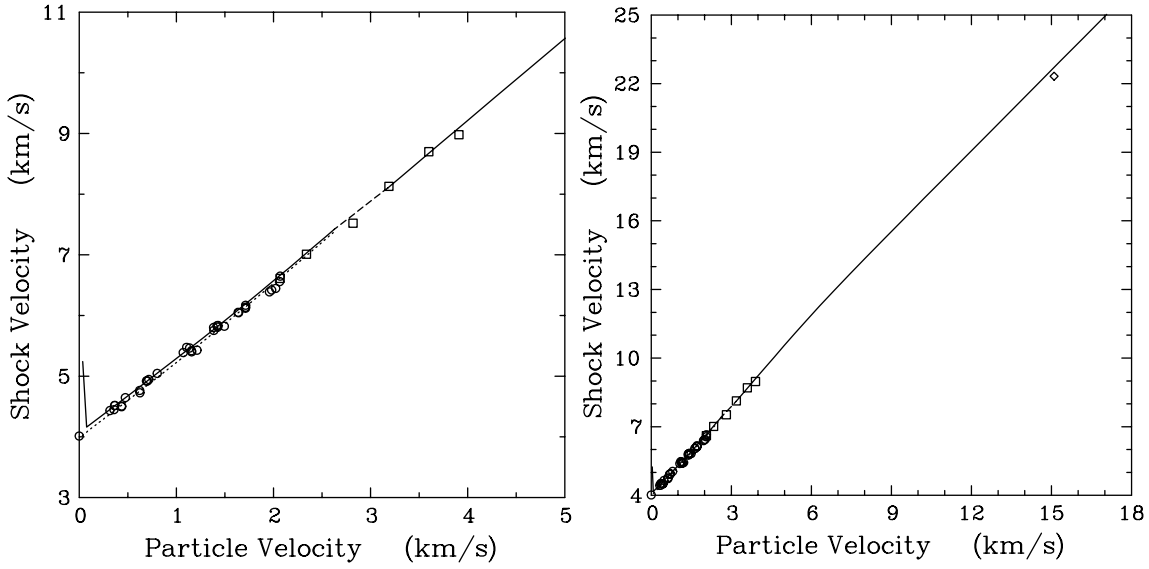

Fig. 13. Tungsten Hugoniot in shock velocity-particle velocity plane. Curves were computed from model; dashed region shows melting region. Left side gives data up to 900 GPa, shown by circles [31] and squares [58]. Right side also gives one data point at 6.5TPa, shown by a diamond [37].

The predicted melting curve and Hugoniot are shown in Fig. 14. The model predicts shock melting to begin at 376 GPa and be complete at 496 GPa. There are no sound speed measurements or other data to test the prediction. The model does not predict a significant change in slope of the Hugoniot in the vicinity of melting. However, the Hugoniot does soften above about 2 TPa. The prediction is well within the error bars of the one melting point at 5 GPa [23].

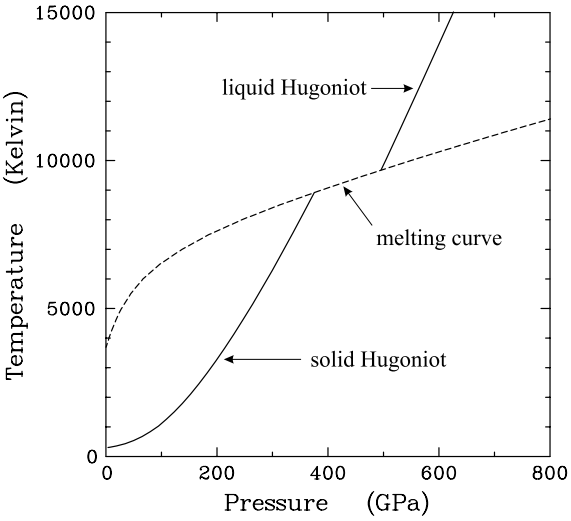

Fig. 14. Calculated melting curve and Hugoniot for W.

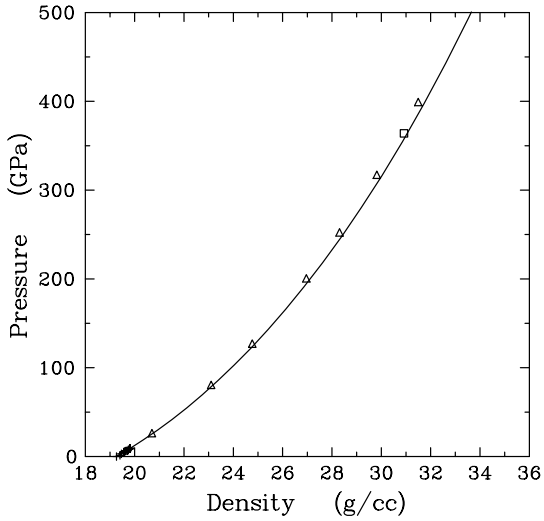

Fig. 15. Room temperature curve for W. Crosses [56], square [57], triangles [60].

Figure 15 compares the predicted room temperature isotherm for tungsten with the static measurements of Ming and Manghnani [56], which go up to 10 GPa, and one high-pressure data point of Ruoff, et al. [57], at 364 GPa. The theoretical calculations of Wang, et al.[60], are shown by triangles.

Chhabildas and Barker give isentropic compression data for tungsten up to 250 GPa [61]. Their data, not shown in Figs. 14 and 15, are quite close to the Hugoniot. However, the isentrope lies above the Hugoniot up to 140 GPa. They assert that the strength effects are larger in the isentropic experiments [62], presumably because of thermal softening in the shocked material.

In constructing the EOS table, Maxwell constructions were included at temperatures above the boiling point, and a tensile region was left at low temperatures for the treatment of spall states. The table covers the density range from 0.0 to 500 g/cc and the temperature range from 5 to 1.0×10^8 K. It has been given material number 3550.

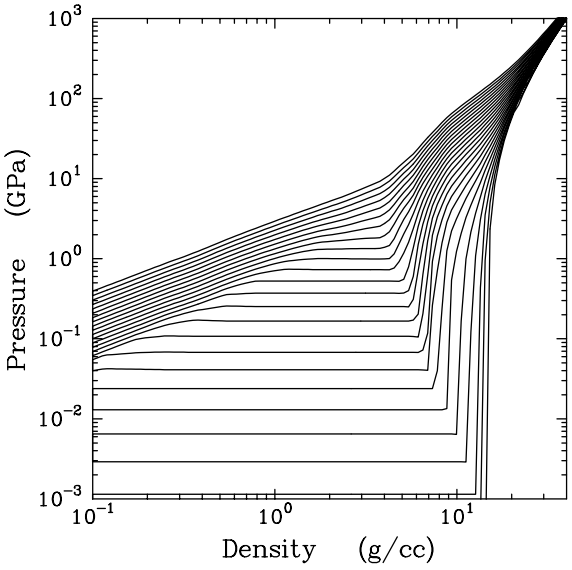

Fig. 16. EOS of tungsten in vapor-liquid transition region. There are 25 isotherms at temperatures from 6000K to 40,000K, equally spaced in the logarithm.

The behavior of the EOS in the vapor-liquid region is shown in Fig. 16. The pressure is plotted as a function of density on 25 isotherms from 6000K to 40,000K. The EOS does not exhibit a PPT, as seen in nickel. However, the metal-insulator transition in the thermal electronic term contributes significantly to the expansion of the liquid phase, as also seen in berylllium. The predicted critical point is at 22500K, 1.6 GPa, and 3.0 g/cc. The critical temperature is somewhat higher than that obtained by other theorists [51], presumably because of our treatment of the thermal electronic term.

Gudarenko, et al., used the impedance matching technique to obtain pressure-particle velocity points on the release isentropes of porous tungsten shocked to two different pressures [53]. The initial density of the samples was 8.87 g/cc. Release isentropes were measured for shock states of 116 and 152 GPa. In contrast to their experiments on nickel (Fig. 11), our EOS shows that the tungsten samples were not shock heated enough to cause much vaporization upon release. Our calculations are compared with their data in Fig. 17. The agreement is satisfactory, except for one data point at 6.39 km/s and 0.058 GPa. This data point indicates a much higher vapor pressure than predicted by our model, a result that we do not consider credible.

Ternovoi, et al. [52], have studied the vaporization behavior of tungsten using a rather complicated experimental configuration designed to obtain data near the critical point. Analysis of their data requires the use of hydrodynamic calculations, which we did not have time to make under the scope of the present effort.

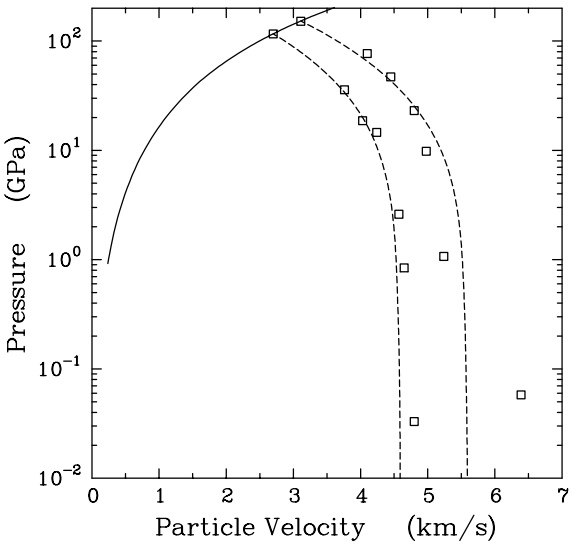

Fig. 17. Expansion isentropes of porous tungsten (initial density 8.87 g/cc). Hugoniot is shown by a solid line, isentropes by dashed lines. Squares are data from [53].

As noted above, many engineering materials are tungsten alloys [63][64]. A typical composition is 90% W by weight, the other elements being Ni, Cu, and Fe. A typical density is 17.0 g/cc, 88% of that for pure tungsten. The scope of the present project did not provide for the development of models for these materials. However, the Hugoniot data for several alloys agree fairly well with the data for pure tungsten—when plotted in the shock velocity-particle velocity plane. As a first approximation, EOS for these alloys can be constructed from the table for pure W, using the density scaling factor in the CTH tabular EOS input [4][5]. (A scaling factor SR=1.13 corresponds to an initial density of 17.04 g/cc.) We offer this recommendation with the following caviat: It will give a reasonable Hugoniot of the alloy, but it should not be expected to give satisfactory predictions for states off the Hugoniot, especially at large expansions and/or high temperatures.

6. Gold

Gold has the fcc structure at RTP [23][24]. No other solid phases have been reported, either at high temperatures or high pressures. Melting occurs at 1337K at zero pressure.

The solid parameters, given in Table 1, were fit to the following experimental data: density [14][20], enthalpy and entropy [16], ultrasonic [65]-[67], static compression [68][69], Hugoniot [31][46][70], and band-theoretical calculations [71]. For the liquid, the tension region of the cold curve was chosen to match the experimental binding energy, and the parameters EFAC and w_{liq} were chosen to match the enthalpy and entropy at the melting point.

The model results are compared to zero-pressure thermophysical and isobaric expansion data in Fig. 18. There are no isobaric expansion data for pure gold; data exist only for a gold-copper alloy (5% Cu) [59][72]. The points shown in Fig. 18 were corrected by normalizing the data to the density, enthalpy, and entropy of pure gold at the melting point. The model predicts higher enthalpies and entropies than observed at high temperatures. We have no explanation for this discrepancy, also seen in our model for Pb [41], at the present time.

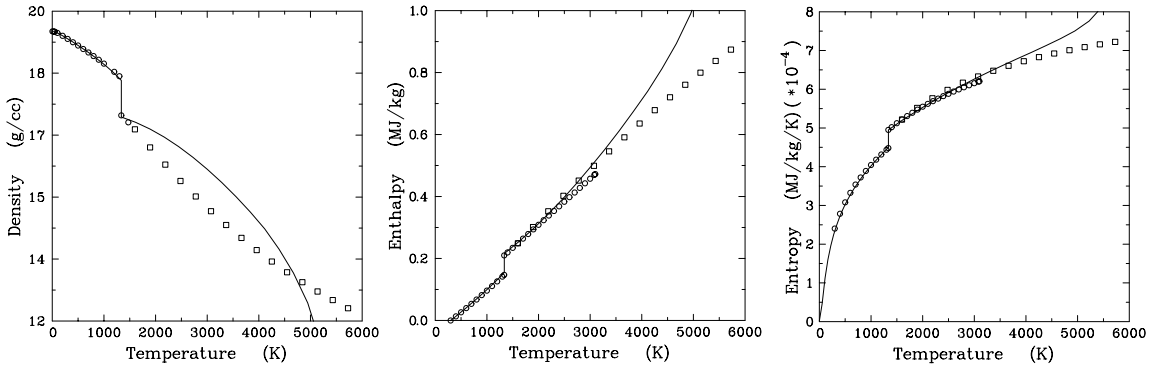

Fig. 18. Comparison of model with thermophysical data for Au. Density: circles—solid and liquid at P=0 [14][20]. Enthalpy and entropy: circles—solid and liquid at P=0 [16]. Squares show isobaric expansion data for a Au-Cu alloy [59][72], modified as described in the text. Solid lines are from model.

The gold Hugoniot is shown in Fig. 19. The left side of the figure compares the calculated curve with the data [31][46][70] up to about 800 GPa. The dashed portion of the curve corresponds to the melting region, 1.84-2.42 km/s. Strength terms were included in computing the Hugoniot in the solid region but have a negligible effect on the results. The right side of the figure shows the Hugoniot up to 1 TPa; there are no experimental data in this region. The model shows a pronounced softening of the Hugoniot upon melting, which is consistent with the

few existing data. Shock data for gold are surprisingly scarce; new measurements would be welcome.

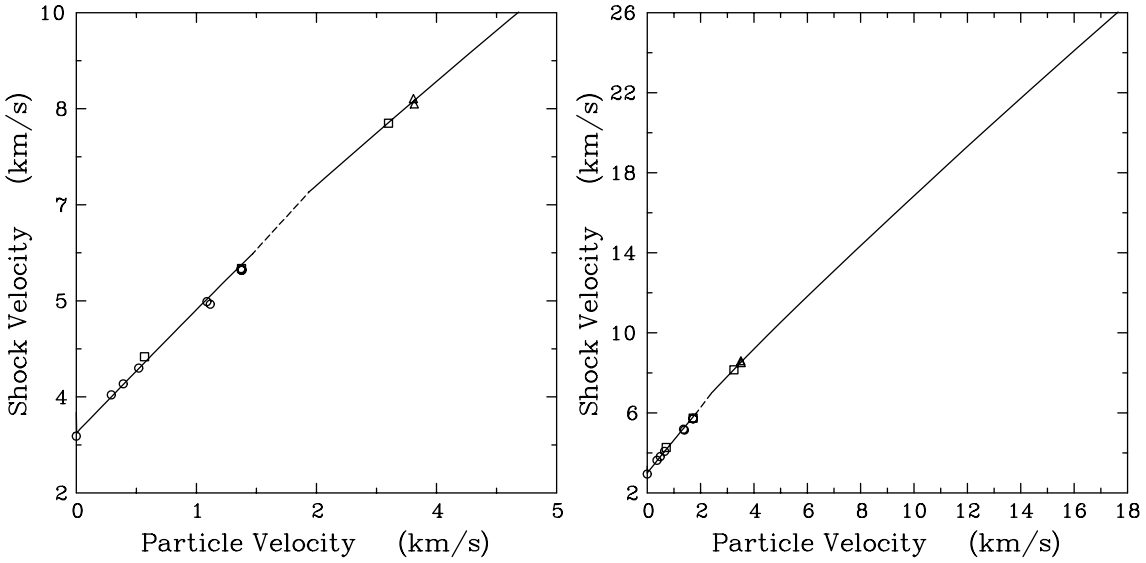

Fig. 19. Gold Hugoniot in shock velocity-particle velocity plane. Curves were computed from model; dashed region shows melting region. Left side gives data up to 800 GPa, shown by circles [31], squares [46], and triangles [70]. Right side extends plot up to 1 TPa.

The predicted melting curve and Hugoniot are shown in Fig. 20. The calculated melting curve is in good agreement with the measurements of Akella and Kennedy [73], which go up to 6.5 GPa. The model predicts shock melting to begin at 212 GPa and to be complete at 328 GPa. There are no sound speed measurements to test the prediction. However, Godwal, et al. [74], have measured the temperature in the shock state at 600 GPa. Their point, shown by a square with error bars in Fig. 20, lies in the liquid range. Our prediction is in satisfactory agreement with their measurement. Godwal, et al., also constructed a theoretical model similar to ours, including use of the CRIS model for the liquid phase. However, our model predicts a higher pressure for melting than theirs. The reason is not obvious, but our model differs from theirs in several respects, including treatment of the thermal electronic terms in the EOS.

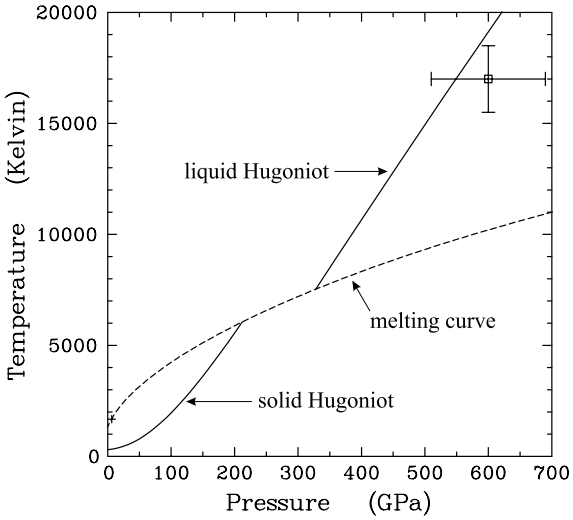

Fig. 20. Calculated melting curve and Hugoniot for Au. Cross shows melting point from [73], square with error bars shows shock temperature measurement from [74].

Figure 21 compares the predicted room temperature isotherm for gold with static measurements [43][68][69] and band-theoretical calculations [71]. Because high-pressure shock data for gold are so scarce, we have used the band-theoretical calculations to fix the value of the cold curve parameter β'_0 given in Table 1.

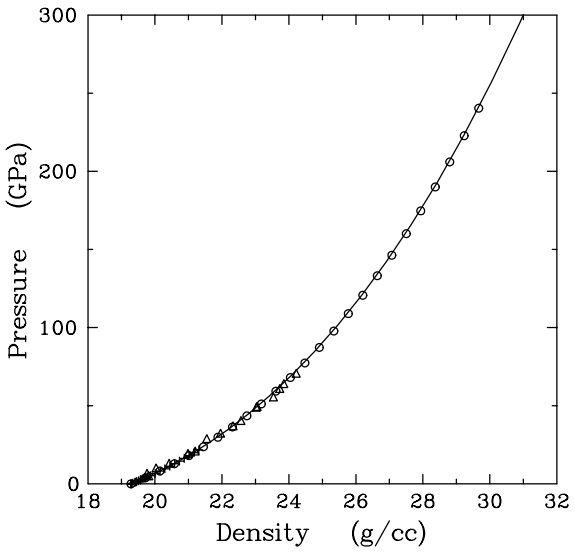

Fig. 21. Room temperature isotherm for gold. Crosses [43][69], diamonds [68], triangles [71].

In constructing the EOS table, Maxwell constructions were included at temperatures above the boiling point, and a tensile region was left at low temperatures for the treatment of spall states. The table covers the density range from 0.0 to 500 g/cc and the temperature range from 5 to 1.0×10^8 K. It has been given material number 2710.

The behavior of the EOS in the vapor-liquid region is shown in Fig. 22. The pressure is plotted as a function of density on 25 isotherms from 3000K to 15,000K. The EOS for Au does not exhibit a PPT like that in Ni. However, the metal-insulator transition in the thermal electronic term does contribute to the expansion of the liquid phase at high temperatures, just as in Be and W. The predicted critical point is at 6200K, 0.45 GPa, and 5.6 g/cc.

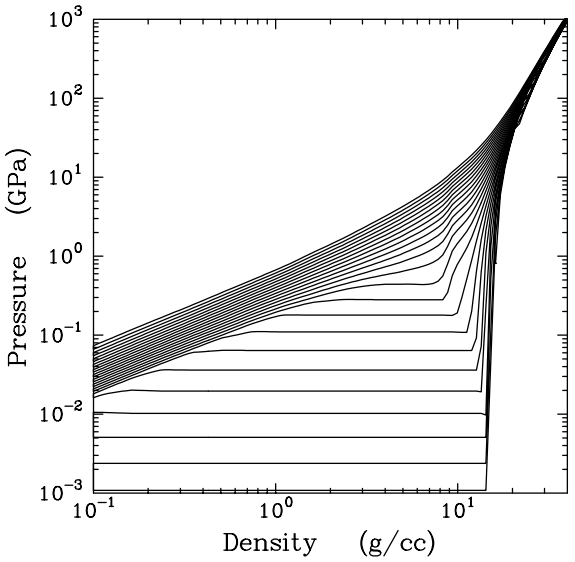

Fig. 22. EOS of gold in vapor-liquid transition region. There are 25 isotherms at temperatures from 3000K to 15,000K, equally spaced in the logarithm.

7. Conclusions and Recommendations

The present report describes new EOS tables for beryllium (material number 2010), nickel (material number 3110), tungsten (material number 3550), and gold (material number 2710). These tables are significantly better than those currently available in the CTH database [7][8]. They should be added to file “sesame” and set as the default materials in the CTH file EOS_dat [4][5].

Experience has shown that no EOS modeling effort is ever fully finished—further refinements are always possible and desirable. In this case, the following tasks are particularly worthy of consideration.

- Further investigation of shock melting is needed for all four metals. No sound speed measurements in the vicinity of melting are available. If such measurements are made, the EOS should be examined to see if they are consistent with them.

- For nickel, as also for aluminum and copper, the model predicts a plasma phase transition in the vapor-liquid critical region. Further theoretical and experimental work is needed to determine if such a transition actually exists and what effect it could have on the material behavior. Analysis of the experiments described in Ref. [52] should also be made.

- EOS models are needed for tungsten alloys, the most common form of tungsten encountered in engineering applications. We have recommended density scaling of the pure tungsten table until better EOS are available. However, this approximation should not be expected to give satisfactory results in all cases.

- Shock wave data for gold are more scarce than for other materials. Revision of this EOS may be required if and when new data become available.

References

[1] J. M. McGlaun, F. J. Ziegler, S. L. Thompson, L. N. Kmetyk, and M. G. Elrick, “CTH - User's Manual and Input Instructions,” Sandia National Laboratories report SAND88-0523, April 1988.

[2] J. M. McGlaun, S. L. Thompson, and M. G. Elrick, “CTH: A Three-Dimensional Shock Wave Physics Code,” Int. J. Impact Engng. 10, 351-360 (1990).

[3] J. M. McGlaun, S. L. Thompson, L. N. Kmetyk, and M. G. Elrick, “A Brief Description of the Three-Dimensional Shock Wave Physics Code CTH,” Sandia National Laboratories report SAND89-0607, July 1990.

[4] E. S. Hertel, Jr. and G. I. Kerley, “CTH EOS Package: Introductory Tutorial,” Sandia National Laboratories report SAND98-0945, 1998.

[5] E. S. Hertel, Jr. and G. I. Kerley, “CTH Reference Manual: The Equation of State Package,” Sandia National Laboratories report SAND98-0947, 1998.

[6] G. I. Kerley, “CTH Equation of State Database: MGRUN Option,” Kerley Publishing Services report KPS00-4, June 2000.

[7] The status of existing EOS models is discussed in several on-line documents in the CTH /data subdirectory. The default EOS tables are discussed in file tables.ref.

[8] G. I. Kerley, “Progress on CTH EOS Database,” memorandum to P. A. Taylor and E. S. Hertel, Jr., June 15, 2000.

[9] G. I. Kerley, ‘‘User’s Manual for PANDA II: A Computer Code for Calculating Equations of State,’’ Sandia National Laboratories report SAND88-2291, 1991.

[10] G. I. Kerley, “Theoretical Equation of State for Aluminum,” Int. J. Impact Engng. **5**, 441-449 (1987).

[11] G. I. Kerley, “Multiphase Equation of State for Iron,” Sandia National Laboratories report SAND93-0027, 1993.

[12] G. I. Kerley, “Equations of State for Titanium and Ti6Al4V Alloy,” Sandia National Laboratories report SAND2003-3785, October 2003.

[13] B. K. Godwal, S. K. Sikka, and R. Chidambaram, “Equation of State Theories of Condensed Matter Up To About 10 TPa,” Phys. Rep. **102**, 121-197 (1983).

[14] Y. S. Touloukian, R. K. Kirby, R. E. Taylor, and T. Y. R. Lee, ‘‘Thermal Expansion, Nonmetallic Solids,’’ Thermophysical Properties of Matter (IFI/Plenum, New York, 1977) Vol. 13.

[15] M. W. Chase, Jr., C. A. Davies, J. R. Downey, Jr., D. J. Frurip, R. A. McDonald, and A. N. Syverud, “JANAF Thermochemical Tables,” J. Phys. Chem. Ref. Data **14**, Supp. No. 1 (1985).

[16] R. Hultgren, P. D. Desai, D. T. Hawkins, M. Gleiser, K. K. Kelley, and D. D. Wagman, *Selected Values of the Thermodynamic Properties of the Elements* (American Society for Metals, Metals Park, Ohio, 1972).

[17] D. A. Liberman, “Self-Consistent Field Model for Condensed Matter,” Phys. Rev. B **20**, 4981-4989 (1979).

[18] G. I. Kerley, “Perturbation Theory and the Thermodynamic Properties of Fluids II. The CRIS Model,” J. Chem. Phys. **73**, 478-486 (1980).

[19] G. I. Kerley, “A Model for the Calculation of Thermodynamic Properties of a Fluid Using Hard-Sphere Perturbation Theory and the Zero-Kelvin Isotherm of the Solid," in Molecular Based Study of Fluids, edited by J. M. Haile and G. A. Mansoori (Am. Chem. Soc., Washington, DC., 1983) pp 107-138.

[20] Handbook of Chemistry and Physics, edited by David R. Lide (CRC Press, Boca Raton, 1996) 77^{th} edition.

[21] G. I. Kerley, ‘‘Theoretical Equations of State for Metals,’’ in Shock Waves in Condensed Matter - 1981, edited by W. J. Nellis, L. Seaman, and R. A. Graham (Am. Inst. of Phys. New York, 1982) pp. 208-212.

[22] G. I. Kerley, “Equations of State for Aluminum and Beryllium,” Kerley Publishing Services report KPS98-1, February 1998.

[23] J. F. Cannon, ‘‘Behavior of the Elements at High Pressures,’’ J. Phys. Chem. Ref. Data 3, 781-824 (1974).

[24] D. A. Young, ‘‘Phase Diagrams of the Elements,’’ Lawrence Livermore Laboratory report UCRL-51902, September 11, 1975.

[25] J. L. Wise, L. C. Chhabildas, and J. R. Asay, ‘‘Shock Compression of Beryllium,’’ in Shock Waves in Condensed Matter - 1981, edited by W. J. Nellis, L. Seaman, and R. A. Graham (Am. Inst. of Phys. New York, 1982) pp. 417-421.

[26] L. C. Chhabildas, J. L. Wise, and J. R. Asay, ‘‘Reshock and Release Behavior of Beryllium,’’ in Shock Waves in Condensed Matter - 1981, edited by W. J. Nellis, L. Seaman, and R. A. Graham (Am. Inst. of Phys. New York, 1982) pp. 422-426.

[27] L. C. Ming and M. H. Manghnani,‘‘Isothermal Compression and Phase Transition in Beryllium to 28.3 GPa,’’ J. Phys. F: Metal Phys. 14, L1-L8 (1984).

[28] L. A. Egorov, A. I. Barenboim, V. V. Mokhova, V. V. Dorohin, and A. I. Samoilov, “X-Ray Diffraction Studies of Structures of Be, Al, LiF, Fe+3%Si, Si, SiO2, KCl Under Dynamic Pressures from 2 GPa to 20 GPa,” J. Phys. IV 7, C3 / 355-C3 / 360 (1997).

[29] D. J. Silversmith and B. L. Averbach, ‘‘Pressure Dependence of the Elastic Constants of Beryllium and Beryllium-Copper Alloys,’’ Phys. Rev B1, 567-571 (1970).

[30] W. D. Rowland and J. S. White,‘‘The Determination of the Elastic Constants of Beryllium in the Temperature Range 25 to 300^{o} C,’’ J. Phys. F: Metal Phys. 2, 232-236 (1972).

[31] S. P. Marsh, LASL Shock Hugoniot Data (University of California, Berkeley, 1980).

[32] F. Perrot, ‘‘Comparison of Various Theoretical Solid-State Models Applied to the Equation of State of Beryllium,’’ Phys. Rev. B 21, 3167-3172 (1980).

[33] D. Liberman, “Equation of State Calculations,” Los Alamos Scientific Laboratory internal memorandum, March 17, 1970.

[34] M. Boivineau, L. Arles, J. M. Vermeulen, and Th. Thevenin, “Thermophysical Properties of Solid and Liquid Beryllium,” Int. J. Thermophys. 14, 427-439 (1993).

[35] W. M. Isbell, F. H. Shipman, and A. H. Jones, “Hugoniot Equation of State of Eleven Elements to Five Mbars,” Materials Science Laboratory report MSL-68-13.

[36] D. J. Steinberg, “Equation of State and Strength Properties of Selected Materials,” Lawrence Livermore National Laboratory report UCRL-MA-106439, Feb. 13, 1991.

[37] C. E. Ragan, ‘‘Shock Compression Measurements at 1 to 7 TPa,’’ Phys. Rev. A25, 3360 (1982).

[38] W. J. Nellis, J. A. Moriarty, A. C. Mitchell, and N. C. Holmes,“Equation of State of Beryllium at Shock Pressures of 0.4-1.1 TPa (4-11 Mbar),” J. Appl. Phys. 82, 2225-2227 (1997).

[39] R. Cauble, T. S. Perry, D. R. Bach, K. S. Budil, B. A. Hammel, G. W. Collins, D. M. Gold, J. Dunn, P. Celliers, L. B. Da Silva, M. E. Foord, R. J. Wallace, R. E. Stewart, and N. C. Woolsey, “Absolute Equation-of-State Data in the 10-40 Mbar (1-4 TPa) Regime,” Phys. Rev. Lett. 80, 1248-1251 (1998).

[40] M. D. Knudson, personal communication.

[41] G. I. Kerley, “Equations of State for Copper and Lead,” Kerley Technical Services report KTS02-1, February 2002.

[42] A. K. McMahan, ‘‘The α–β Transition in T=0 High Pressure Beryllium,’’ in Shock Waves in Condensed Matter - 1981, edited by W. J. Nellis, L. Seaman, and R. A. Graham (Am. Inst. of Phys. New York, 1982) pp. 340-344. The unpublished data were provided to us for purposes of comparison.

[43] S. N. Vaidya and G. C. Kennedy, ‘‘Compressibility of 18 Metals to 45 kbar,’’ J. Phys. Chem. Solids 31, 2329 (1970).

[44] L. V. Al’tshuler, A. A. Bakanova, and R. F. Trunin, “Shock Adiabats and Zero Isotherms of Seven Metals at High Pressures,” Sov. Phys. JETP 15, 65 (1968).

[45] S. B. Kormer, A. I. Funtikov, V. D. Urlin, and A. N. Kolesnikova, “Dynamic Compression of Porous Metals and the Equation of State With Variable Specific Heat at High Temperatures,” Sov. Phys. JETP 15, 477 (1962).

[46] L. V. Al'tshuler, A. A. Bakanova, L. P. Dudoladov, E. A. Dynin, R. F. Trunin, and B. S. Chekin, "Shock Adiabatic Curves of Metals. New Data, Statistical Analysis, and General Laws," Sov. J. Appl. Mech. Tech. Phys. 22, 145-169 (1981).

[47] A. K. McMahan and R. C. Albers,‘‘Insulating Nickel at 340 Million Atmospheres of Pressure,’’ Phys. Rev. Lett. 49, 1198 (1982).

[48] D. J. Andrews, “Equation of State of the Alpha and Epsilon Phases of Iron,” J. Phys. Chem. Solids 34, 825-840 (1973).

[49] W. Obendrauf, E. Kaschnitz, G. Pottlacher, and H. Jager, “Measurements of Thermophysical Properties of Nickel with a New Highly Sensitive Pyrometer,” Int. J. Thermophys. 14, 417-427 (1993).

[50] R. S. Hixson, M. A. Winkler, and W. M. Hodgdon, “Sound Speed and Thermophysical Properties of Liquid Iron and Nickel,” Phys. Rev. B42, 6485-6491 (1990).

[51] P. R. Levashov, V. E. Fortov, K. V. Khishchenko, and I. V. Lomonosov, “Equation of State for Liquid Metals,” in Shock Compression of Condensed Matter - 1999, edited by M. D. Furnish, L. C. Chhabildas, and R. S. Hixson (AIP Conference Proceedings 505, 2000) pp. 89-92.

[52] V. Ya. Ternovoi, A. S. Filimonov, V. E. Fortov, S. V. Kvitov, D. N. Nikolaev, and A. A. Pyalling, “Liquid-Vapor Phase Boundaries Determination by Dynamic Experimental Method,” in Shock Compression of Condensed Matter - 1999,

edited by M. D. Furnish, L. C. Chhabildas, and R. S. Hixson (AIP Conference Proceedings 505, 2000) pp. 189-192.

[53] L. F. Gudarenko, O. N. Gushchina, M. V. Zhernokletov, A. B. Medvedev, and G. V. Simakov, "Shock Compression and Isentropic Expansion of Tungsten, Nickel and Tin Porous Samples," in Shock Compression of Condensed Matter - 1999, edited by M. D. Furnish, L. C. Chhabildas, and R. S. Hixson (AIP Conference Proceedings 505, 2000) pp. 193-196.

[54] D. I. Bolef and J. de Klerk, "Elastic Constants of Single-Crystal Mo and W Between 77º and 500º K," J. Appl. Phys. 33, 2311-2314 (1962).

[55] F. H. Featherston and J. R. Neighbours, "Elastic Constants of Tantalum, Tungsten, and Molybdenum," Phys. Rev. 130, 1324-1333 (1963).

[56] L. Ming and M. H. Manghnani, "Isothermal Compression of bcc Transition Metals to 100 kbar," J. Appl. Phys. 49, 208-212 (1978).

[57] A. L. Ruoff, H. Xia, H. Luo, and Y. K. Vohra, "Miniaturization Techniques for Obtaining Static Pressures Comparable to the Pressure at the Center of the Earth: X-Ray Diffraction at 416 GPa," Rev. Sci. Instrum. 61, 3830-3833 (1990).

[58] R. S. Hixson and J. N. Fritz, "Shock Compression of Tungsten and Molybdenum," J. Appl. Phys. 71, 1721-1728 (1991).

[59] G. R. Gathers, "Dynamic Methods for Investigating Thermophysical Properties of Matter at Very High Temperatures and Pressures," Rep. Prog. Phys. 49, 341-396 (1986). Two sets of data are given for tungsten. Data from table 12 (Kiel) is shown by squares in Fig. 12. Data from table 32 (Livermore) is shown by circles in Fig. 12.

[60] Y. Wang, D. Chen, and X. Zhang, "Calculated Equation of State of Al, Cu, Ta, Mo, and W to 1000 GPa," Phys. Rev. Lett. 84, 3220-3223 (2000).

[61] L. C. Chhabildas, and L. M. Barker, ''Dynamic Quasi-Isentropic Compression of Tungsten,'' in Shock Waves in Condensed Matter - 1987, edited by S. C. Schmidt and N. C. Holmes (North-Holland, Amsterdam, 1988) pp. 111-114. Note that the isentrope is very close to the Hugoniot for W.

[62] L. C. Chhabildas, J. R. Asay, and L. M. Barker, ''Shear Strength of Tungsten Under Shock- and Quasi-Isentropic Loading to 250 GPa,'' Sandia National Laboratories report SAND88-0306, 1988. - strength data in this report appear to be consistent with Steinberg's parameters.

[63] M. van Thiel, Editor, "Compendium of Shock Wave Data," Lawrence Livermore Laboratory report UCRL-50108, Rev. 1, June 1977. Data are given for three W-Ni-Cu alloys.

[64] G. E. Hauver, “The Hugoniot for 90W-7Ni-3Fe Tungsten Alloy,” Ballistic Research Laboratory report ARBRL-MR-02987, February 1980.

[65] J. R. Neighbours and G. A. Alers, ‘‘Elastic Constants of Silver and Gold,’’ Phys. Rev. 111, 707-712 (1958).

[66] W. B. Daniels and C. S. Smith, ‘‘Pressure Derivatives of the Elastic Constants of Copper, Silver, and Gold to 10,000 Bars,’’ Phys. Rev. 111, 713-721 (1958).

[67] Y. Hiki and A. V. Granato, ‘‘Anharmonicity in Noble Metals: Higher Order Elastic Constants,’’ Phys. Rev. 144, 411-419 (1966).

[68] D. L. Heinz and R. Jeanloz, ‘‘The Equation of State of the Gold Calibration Standard,’’ J. Appl. Phys. 55, 885-893 (1983).

[69] L. C. Ming, D. Xiong, and M. H. Manghnani, ‘‘Isothermal Compression of Au and Al to 20 GPa,’’ Physica 139 & 140B, 174-176 (1986).

[70] Data of Jones, et al., as reported in Ref. [63].

[71] B. K. Godwal and R. Jeanloz, ‘‘First-Principles Equation of State of Gold,’’ Phys. Rev. B 40, 7501-7507 (1989).

[72] W. M. Hodgson, ‘‘Equation of State and Transport Measurements on Expanded Liquid Metals Up to 8000 ^{o}K and 0.4 GPa,’’ Ph.D. Thesis, Lawrence Livermore Laboratory report UCRL-52493, May 1978.

[73] J. Akella and G. C. Kennedy, “Melting of Gold, Silver, and Copper—Proposal for a New High-Pressure Calibration Scale,” J. Geophys. Res. 76, 4969-4977 (1971).

[74] B. K. Godwal, A. Ng, and L. DaSilva, “Shock Melting and Hugoniot Calculations for Gold,” Phys. Lett. A 144, 26-30 (1990).

[75] G. I. Kerley, “Theory of Ionization Equilibrium: An Approximation for the Single Element Case,” J. Chem. Phys. **85**, 5228-5231 (1986).

[76] G. I. Kerley and L. C. Chhabildas, “Multicomponent-Multiphase Equation of State for Carbon,” Sandia National Laboratories report SAND2001-2619, 2001.

[77] G. I. Kerley, “Atomic Orbital Data for Elements with Atomic Numbers $1 \leq Z \leq 103$,” Sandia National Laboratories report SAND88-2594, 1988.

[78] R. D. Cowan, *The Theory of Atomic Structure and Spectra* (University of California, Berkeley, 1981) pp. 12-15.

[79] G. I. Kerley, “Modification of the Lee-More Conductivity Model: Improved Calculation of Ionization State,” Kerley Publishing Services report KPS99-2, Albuquerque, NM, February 1999.

Appendix A

Thermal Electronic Contributions

The thermal electronic contributions to the EOS, subscripted *e* in Eqs. (1)-(3) and (6), typically become significant in metals at temperatures above 1000-2000K, particularly for expanded states. The theory of many-electron systems is still not completely solved, and drastic approximations must be made to obtain tractable computational models. Existing models fall into two main types, neither of which gives satisfactory results over the entire range of interest.

- A model that uses an explicit sum over all electronic configurations of the system is normally the best choice at low densities. The PANDA ionization equilibrium model (IEQ) [9] falls into this category.
- A model that uses an average electronic configuration, with an accurate calculation of the energy levels, is normally the best choice at high densities. The INFERNO model of Liberman [17] falls into this category.

In previous work, we have obtained satisfactory results by merging calculations from the PANDA IEQ model at low densities with the INFERNO model at high densities [10][11]. However, smoothing is required to obtain a single table that is well behaved in the transition region. In this work, the IEQ model was used for densities below the metal-insulator transition, and a modified version of INFERNO was used at higher densities. Details are given below.

IEQ Calculations

The PANDA IEQ model uses an approximate form of the ionization equilbrium equations that considers an “average atom” but explicitly sums over all electronic configurations and states of ionization. This procedure has been shown to avoid the errors in statistical weights that arise from using an “average” configuration, as is done in many other models, including INFERNO [75]. The model also includes continuum lowering and pressure ionization. The original version of the model is discussed in Sec. 9 of the PANDA manual [9]. The version used in this work includes two improvements—corrections for charge fluctuations and for thermal broadening. These new features are described in a recent report on the carbon EOS [76].

The IEQ model also uses a scaling model for computing ionization potentials, energy levels, statistical weights, and continuum lowering parameters from a table of atomic orbital data. Reference [77] gives orbital parameters for all elements up through atomic number 103. As in previous work, the orbital energies for all four metals were modified to improve agreement with the experimental ionization potentials [78]. Small changes to the orbital energies for unoccupied states were also

made to improve agreement with the amount of thermal excitation predicted by INFERNO.

The IEQ results were generated using the following parameter settings.

- MX=EFAC=3. MX is the maximum number of electron-hole excitations from the ground state, and EFAC is the energy cutoff, relative to the ionization energy, in the sum over excited states. These factors are large enough to include all important contributions to the ion partition functions.
- F1=F2=1. We chose the default values for these factors, used in the continuum lowering model, because the results are relatively insensitive to them below the metal-insulator transition.
- F3=0.1. This constant, used in the average atom corrections, was the same as we have used in calculations for other materials [76][79].
- The constant XB, used in the thermal broadening model [76], was chosen to get a reasonable amount of smoothing.

The entropy was computed at 35 temperatures, exponentially spaced on the interval $2.3 \times 10^3 \le T \le 1.16 \times 10^8 K$, and T=0 points obtained by extrapolation. The density mesh for each material ranged from 1.0×10^{-9} g/cc to a value above the metal-insulator transition, with 6 points per decade.

INFERNO Calculations

The INFERNO model uses a spherical atom, embedded in a homogeneous electron gas, to approximate the electronic structure of condensed matter. The atomic radius is determined by the density (Wigner-Seitz formula), and the electron gas is used to represent the surrounding atoms. The self-consistent-field approximation is used to compute both the bound and free energy levels. INFERNO considers an average configuration, using Fermi-Dirac statistics to compute the orbital occupation numbers, the electron screening contribution to the potential, and the thermodynamic functions. The energy levels are computed by numerical solution of the Dirac equation with a local exchange-correlation potential; this procedure treats the bound and free orbitals consistently and predicts smooth behavior when orbitals are pressure-ionized.

In order to compute the EOS, it is necessary to separate the terms belonging to the atom from those belonging to the electron gas. INFERNO offers several prescriptions for this separation. In order to ensure thermodynamic consistency, we use only the entropy data, calculating the other thermodynamic functions by the method discussed in Sec. 8 of the PANDA manual [9]. Of the two entropy formulas, we prefer the so-called “model A” expression. (“Model T” gives similar results to model A, but sometimes yields negative entropies at low temperatures.) The model A formula can be written

$$S_e = (R/W)\left[\sum_b X_b \ln w_b + \int_\kappa X_\kappa \ln w_\kappa d\kappa\right], \tag{11}$$

Where the sum is taken over the bound states and the integral is taken over the free states having wavevectors κ. Here w_i is the statistical weight of level *i*, and X_i is the fraction of the electron density inside the atomic sphere. INFERNO uses the Fermi-Dirac expression for the statistical weight,

$$\ln w_i = -g_i[p_i \ln(p_i) + (1-p_i)\ln(1-p_i)], \tag{12}$$

$$p_i = \{1 + \exp[(\varepsilon_i - \mu)/kT]\}^{-1}, \tag{13}$$

where g_i is the degeneracy of the level, ε_ι is the energy of the level, and μ is the chemical potential.

Although Eq. (12) is well-known and widely-used, it is only an approximation. As we will show below, it does not give the correct weights for the bound states of the atom (except for filled levels) and this error leads to a mismatch with the IEQ model at low densities. In past work, we have modified the IEQ results to match INFERNO, in order to smooth the transition between the two models. However, this approach propagates the statistical weight error, which can introduce error in the calculated vapor pressure. Since the IEQ model gives the correct results at low densities, we seek a way to modify the INFERNO model in this regime.

In order to understand this problem—and how to correct it—we must pay more careful attention to the statistical weight of a bound level. Let *g* be the degeneracy and *n* the occupation number of a level. The statistical weight is given by the binomial coefficient

$$w = g!/n!(g-n)! \tag{14}$$

Application of Stirling's formula for factorials leads to Eq. (12)—for *large* values of *g* and *n*. For small values of *g* and *n*, a more accurate expression is

$$\ln w \cong -f(g,p)\,g[p\ln p + (1-p)\ln(1-p)], \tag{15}$$

where $p = n/g$. Actual calculations show that $0.5 \le f \le 1.0$. A good approximation to the function *f* is

$$f(g,p) \cong 1 + \frac{1}{2g}\frac{\ln p + \ln(1-p) + \ln(2\pi g + 16 - 4\pi)}{p\ln p + (1-p)\ln(1-p)}. \tag{16}$$

Note that Eq. (12) is correct to within a factor of 2 and is exact for large values of *g*.

We also note that $f = 1$ for the free states, because the continuum wave functions extend throughout the system and the degeneracy is virtually infinite.

As an example, consider a gas of hydrogen atoms, all in the ground state. Since each atom has one electron and two spin states (g=2, n=1), the statistical weight is w=2. By contrast, Eqs. (12) and (13) give p=1/2 and w=4, which is incorrect. Equation (15) gives the correct result.

We cannot simply replace Eq. (12) by Eq. (15) for $\ln w_b$ in Eq. (11); to do so would neglect fluctuations about the average configuration. It is known from statistical mechanics that such fluctuations are negligible for a large number of electrons. However, they cannot be neglected for a small number of electrons. Fluctuations will be especially important at high temperatures. Even at low temperatures, they are important when two levels, e.g., 3D- and 3D+, are close in energy. In such cases, one should sum the degeneracies of both levels when computing an appropriate value of $f(g, p)$.

A solution to the problem of fluctuations is beyond the scope of this work, and we have had to resort to a simple expedient. Our principal objective is to obtain a smooth transition between the IEQ and INFERNO models while retaining the IEQ results at low temperatures and densities. This objective can be attained by modifying the INFERNO entropy formula, Eq. (11), as follows.

$$S_e = (R/W)\left[\sum_b Y_b X_b \ln w_b + \int_\kappa X_\kappa \ln w_\kappa d\kappa\right], \tag{17}$$

$$Y_b = f + (1-f)\exp(\varepsilon_b/kT), \tag{18}$$

where f is a constant, and ε_b is the energy of level b, relative to the bottom of the continuum. The same value of f is used for all levels; it is chosen to match the IEQ results at low temperatures. The exponential factor ensures that $Y_b \to 1$ at high temperatures or when a bound state crosses into the continuum. Because this procedure treats the bound and free states differently, it introduces small fluctuations in the entropy in the neighborhood of bound-free transitions. However, this structure is smoothed out after thermal broadening is applied.

INFERNO calculations for the four metals were carried out using version 41 of the code, obtained from D. A. Liberman, with the above modifications. The entropy was computed at 35 temperatures, exponentially spaced on the interval $2.3 \times 10^3 \le T \le 1.16 \times 10^8 K$, and T=0 points obtained by extrapolation. The density mesh for each material ranged from a value below the metal-insulator transition to a maximum value 20 times the atomic weight, with 12 points per decade.

Merged Electronic Table

The IEQ and INFERNO calculations were merged into a single entropy table for use in the solid and liquid models. The IEQ results were used at low densities, below the metal-insulator transition, and the INFERNO results were used at higher densities. All of the other thermodynamic functions were computed from the entropy table, as explained in Sec. 8 of the PANDA manual. PANDA uses the TFD model when it is out of range of the entropy table.

As noted above, the parameter *f* in Eq. (18) was used to match the INFERNO results to the IEQ results at low temperatures. However, this procedure still leaves small differences between the two data sets at the match density; if not corrected, these discrepancies lead to spurious structure in the pressure, which is computed by differentiation. In order to eliminate this problem, the IEQ entropies at each temperature were shifted by a constant chosen to match the INFERNO entropies at the match density. The thermal broadening option was also applied to smooth any remaining structure.

The thermal electronic contributions to the entropy and pressure for tungsten are shown in Fig. 23. The most striking feature of the plots is the metal-insulator transition that occurs in the density range 6-12 g/cc. At low densities, the valence electrons are localized, insulating states. At low temperatures, the transition to delocalized, metallic behavior with increasing density first causes a rise in entropy as the ionization energy decreases, then a drop in the entropy as the electrons become more free. The thermal electronic pressure is negative below the transition and positive above it.

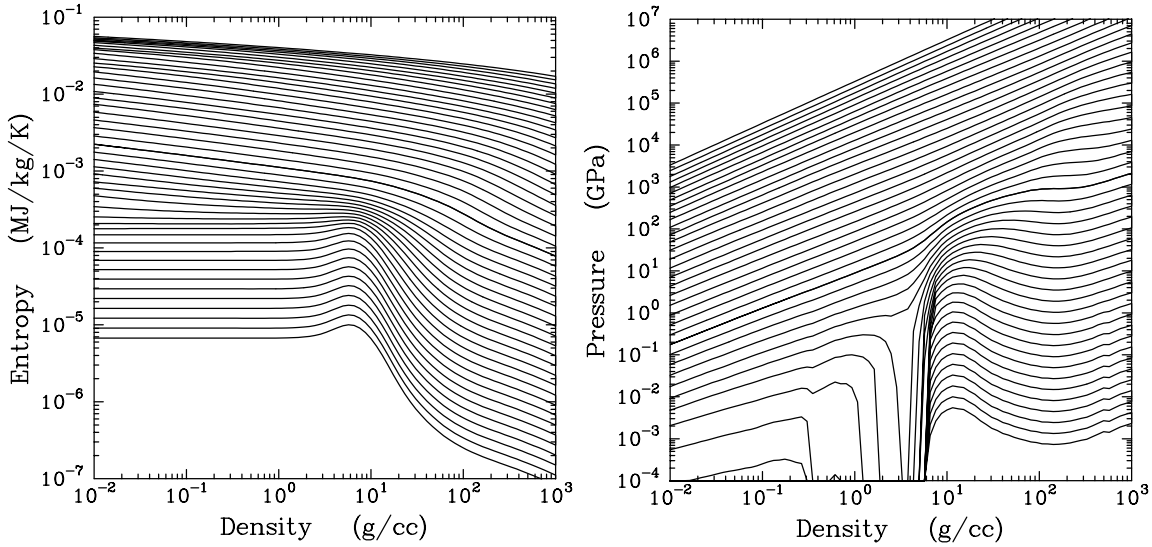

Fig. 23. Thermal electronic entropy and pressure for W. Each plot shows 49 isotherms at temperatures from 100 to 10^8K, equally spaced in the logarithm.

This phenomenon has a significant effect on the heat capacity and thermal expansion of metals at temperatures above 2000K, affecting both the thermal expansion and the heat capacity. The details of the behavior are strongly dependent on the amount of thermal broadening. In some cases, it leads to a plasma phase transition (PPT) in the vicinity of the vapor-liquid critical point, even when a large amount of thermal broadening is applied.

In this work, Ni is predicted to have a PPT, while Be, W, and Au are not. Our model also predicts a PPT in Cu but not in Pb [41].

Appendix B

Plots of Tension Region

The following plots have been included in response to a request for more information about the tension region of the tables. All EOS models that have a realistic treatment of the vapor-liquid transition display van der Waals loops at low temperatures. The equilibrium vapor-liquid transition is described by the "Maxwell construction." At a given temperature, the two-phase region is defined by the densities at which the vapor and liquid have equal pressures and Gibbs free energies. The pressure is constant in the two-phase region, while the energy is given by a volume-weighted average.

In generating an EOS table, we normally include the Maxwell constructions at temperatures above the boiling point but allow a tension region at low temperatures so that the EOS can be used in hydrocode calculations that treat spallation behavior. Unfortunately, the inconsistency inherent in this procedure leads to negative heat capacities and other numerical problems at densities below the liquid spinodals. PANDA eliminates this problem by substituting well-behaved functions at low temperatures and densities. (See Sec. 13.5 of the PANDA manual [9].)

The resulting tension regions for Be, Ni, W, and Au are shown in Fig. 24. Given the typical tensile strengths for these materials (Be—0.35 GPa, Ni—2.0 GPa, W—0.9 GPa, Au—0.12 GPa), the tables should give a reasonable description of spallation behavior in most cases. In unusual cases, i.e., where a material is very hot when it goes into tension, it may be necessary to use a temperature-dependent fracture model or simply reduce the fracture strength to avoid getting into the artificial region.

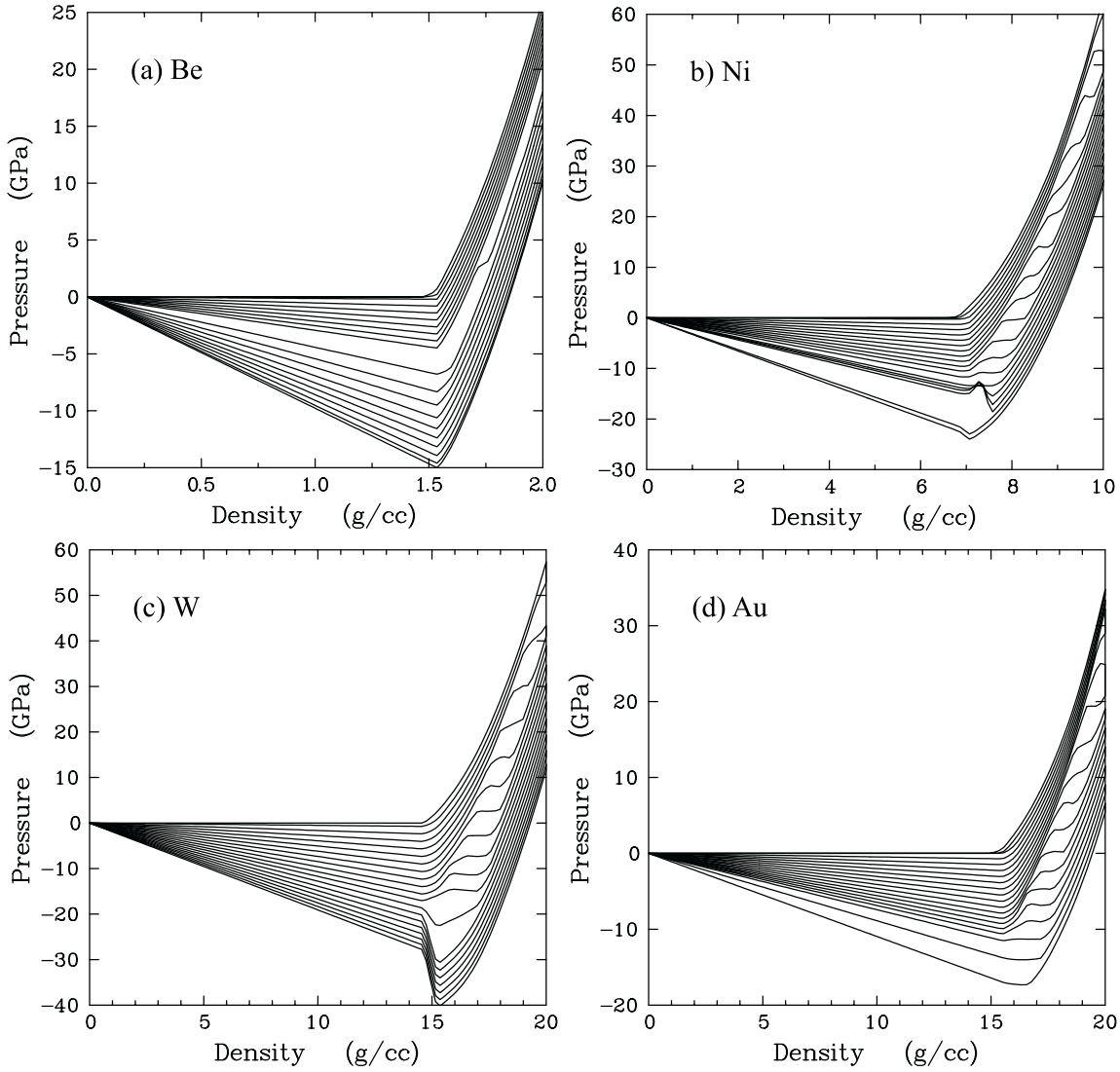

Fig. 24. Plots of tension region for Be, Ni, W, and Au. There are 20 isotherms, equally spaced in temperature, covering the following ranges: Be, 100-3000K; Ni, 100-3500K; W, 100-6000K; Au, 100-3500K.

Distribution

1 Alliant TechSystems
Attn: Frederick Stecher
MS: MN07-MW44
4700 Nathan Lane N.
Plymouth, MN 55442-2512

3 Applied Research Associates, Inc.
Attn: Dennis Grady
Craig Doolittle
K. Bryan Milligan
4300 San Mateo Blvd. NE, Suite A-220
Albuquerque, NM 87110

1 Applied Research Associates, Inc.
Attn: William Brown
2760 Eisenhower Ave., Suite 308
Alexandria, VA 22314

1 Applied Research Associates
Attn: Peter Dzwilewski
5941 South Middlefield Rd., Suite 100
Littleton, CO 80123

2 Battelle Memorial Institute
Attn: Dale Trott
Mike Fisher
505 King Ave.
Columbus, OH 43201-2693

1 Boeing Corporation
Attn: Kevin Housen
MS 2T-50
P. O. Box 3999
Seattle, WA 98124

1 Boeing Company
Attn: Irene Aronoff
MC QB-62
PO Box 7922
Canoga Park, CA 91309-7922

1 Brown University
Attn: Peter Schultz
Dept. of Geological Sciences
P.O. Box 1846
Providence, RI 02912

1 Brigham Young University
Attn: Carl Sorenson
Dept. of Mech. Engineering
Provo, UT 84602

1 California Institute of Technology
Attn: Thomas Ahrens
Seismological Laboratory
1299 E. California Blvd.
Pasadena, CA 91125

1 California Institute of Technology
Attn: Joseph Shepherd
Engineering and Applied Science
MC 105-50
Pasadena, CA 91125

3 Carnegie Institution of Washington
Geophysical Laboratory
Attn: T. S. Duffy
R. M. Hemley
H. K. Mao
5251 Broad Branch Rd., NW
Washington, DC 20015

1 Cornell University
Department of Physics
Attn: Neil W. Ashcroft
Ithaca, NY 14853

1 Cornell University
Materials Science & Engineering
Attn: Arthur L. Ruoff
Ithaca, NY 14853

1 Enig Associates, Inc.
Attn: Julius W. Enig
11120 New Hampshire Ave., Suite 500
Silver Spring, MD 20904-26

1 Harvard University
Attn: Sarah Stewart-Mukhopadhyay
Department of Earth & Planetary Sciences
Cambridge, MA 02138

1 Institute for Defense Analyses
Attn: Bohdan Balko
1801 North Beauregard Street
Alexandria, VA 22311

15 Kerley Technical Services
Attn: Gerald I. Kerley, Consultant
P.O. Box 709
Appomattox, VA 24522-0709

1 KTech
Attn: Larry Lee
2201 Buena Vista SE, Suite 400A
Albuquerque, NM 87106-4265

2 Lockheed Martin Missiles Space Systems
Missiles & Space Operations
Attn: Erik Matheson
Luen Tam
1111 Lockheed Martin Way
Sunnyvale, CA 94089

2 NASA Johnson Space Center
Attn: Eric L. Christiansen
Justin H. Kerr
Mail Code SN3
Houston, TX 77058

2 NASA/Langley Research Center
Attn: Scott A. Hill, MS 431
Carl Poteet, MS 396
1 North Dryden St.
Hampton, VA 23681-2199

5 Naval Air Warfare Center
Attn: Joseph B. Bickley
Thomas J. Gill
John Kandell
Kelly Minnick
Edwin Szymanski
1 Administrative Circle
China Lake, CA 93555

1 Naval Postgraduate School
ELectrical & Computer Engineering Dept.
Attn: Donald Wadsworth
833 Dyer Road, Bldg. 232
Monterey, CA 93943-5121

7 Naval Surface Warfare Center
Dahlgren Division
Attn: J. R. Cogar
R. Gamache
R. K. Garrett, Jr.
M. Hobson
D. F. Robinson
D. Vavrick
L. T. Wilson
17320 Dahlgren Rd.
Dahlgren, VA 22448

6 Naval Surface Warfare Center
Indian Head Division
Attn: Bill Lawrence
Phil Miller
Thomas P. Russell
Gerrit Sutherland
Daniel Tam
Frank J. Zerilli
101 Strauss Avenue
Indian Head, MD 20640-5035

2 Network Computing Services, Inc.
AHPCRC
Attn: Gordon R. Johnson
Tim Holmquist
1200 Washington Avenue South
Minneapolis, MN 55415

1 New Mexico State Inst. of Mining & Tech.
Attn: Robert Abernathy
EMRTC Center
Socorro, NM 87801

1 Oak Ridge National Laboratory
Attn: Seokho Kim
P. O. Box 2009
Oak Ridge, TN 37831-8045

1 Plattsburgh State University
Department of Physics
Attn: Paul P. Szydlik
101 Broad Street
Plattsburg, NY 12901-2681

1 Schlumberger Reservoir Completions
Center, Perforating Gun Systems
Attn: Wenbo Yang
14910 Airline Road
Rosharon, TX 77583

1 Science Applications International Corp.
Attn: Gerry Gurtman
10260 Campus Point Drive
San Diego, CA 92121

1 Science Applications International Corp.
Attn: Mark E. Beyers
1710 SAIC Drive
McLean, VA 22102

2 Southwest Research Institute
Attn: Charles E.Anderson
James Walker
P. O. Drawer 28510
San Antonio, TX 78228-0510

1 Texas A&M University
Nuclear Engineering Dept.
Attn: Bruce L. Freeman
Zachry Building, Room 129
College Station, Texas 77843-3133

1 Texas Tech University
Department of Mechanical Engineering
Attn: Darryl James
Box 41021
Lubbock, TX 79409-1021

2 Thiokol Corporation
Science & Engineering Division
Attn: Robert L. Hatch, Mailstop 244
Dwight Clark, Mailstop 280
P. O. Box 707
Brigham City, Utah 84302-0707

1 University of Alabama in Huntsville
Aerophysics Department
Attn: Mark Zweiner
P.O. Box 999
Huntsville, AL 35899

2 University of Arizona
Department of Planetary Sciences
Attn: W. B. Hubbard
H. J. Melosh
Tucson, AZ 85721

1 University of California
Attn: Raymond Jeanloz
Earth and Planetary Science
Berkeley, CA 94720-4767

15 University of California
Lawrence Livermore National Laboratory
Attn: R. Cauble
G. W. Collins
H. C. Graboske
J. Heidrich
N. C. Holmes
B. Militzer
B. Moran
J. A. Moriarty
A. K. McMahan
W. J. Nellis
P. C. Souers
C. M. Tarver
S. T. Weir
D. A. Young
G. B. Zimmerman
P.O. Box 808
Livermore, CA 94550

18 University of California
Los Alamos National Laboratory
Attn: Chris Adams
J. Boettger
L. A. Collins
L. L. Davis
R. Gustavsen
R. S. Hixson
B. L. Holian
Y. Horie
J. D. Johnson
J. E. Kennedy
J. D. Kress
J. Mace
E. S. Martin
R. Parker
J. M. Pedicini
J. P. Ritchie
S. Sheffield
D. Saumon
P.O. Box 1663
Los Alamos, NM 87545

1 University of Illinois
Attn: David M. Ceperley
Department of Physics
1110 W. Green Street
Urbana, IL 61801

1 University of Missouri-Rolla
CE Department
Attn: William Schonberg
Rolla, MO 65409

1 University of Notre Dame
Dept. of Aerospace and Mech. Eng.
Attn: Joseph M. Powers
372 Fitzpatrick Hall of Engineering
Notre Dame, Indiana 46556-5637

1 University of Rochester
Laboratory for Laser Energetics
Attn: R. L. McCrory
250 East River Road
Rochester, NY 14623-1299

1 University of Rochester
Physics & Astronomy
Attn: Hugh M. Van Horn
RC Box 270171
Rochester, NY 14627-0171

2 The University of Texas at Austin
Institute for Advanced Technology
Attn: Stephan J. Bless
David Littlefield
4030 W. Braker Lane, Suite 200
Austin, TX 78712

1 University of Texas at El Paso
Mechanical & Industrial Engineering
Attn: Michael Huerta
500 West University Avenue
El Paso, TX 79968

1 University of Washington
Dept. of Aeronautics and Astronautics
Attn: Keith A. Holsapple, FS10
Seattle, WA 98195

1 U.S. Air Force Inst. of Technology/ENY
Attn: Jay R. Anderson
Wright-Patterson AFB, OH 45433

1 U.S. Air Force Research Laboratory
Attn: David F. Medina
3550 Aberdeen Ave SE
Kirtland AFB, NM 87117-5776

10 U.S. Army Research Laboratory
Attn: W. Bruchey
D. Dandekar
F. Gregory
A. D. Gupta
Y. Huang
K. D. Kimsey
H. Meyer, Jr.
M. L. Normandia
S. Schoenfeld
J. Starkenberg
P.O. Box 334, Main Station
Aberdeen Proving Ground, MD 21005

3 U.S. Army Space & Missile Defense Command
Attn: Robert Becker
Jason McCullough
Tim Reid
PO Box 1500
Huntsville, AL 35807-3801

2 U. S. Army TACOM-ARDEC
SMCAR-AEE-WW
Attn: Ernest L. Baker
Chuck Chin
Picatinny Arsenal, NJ 07806-5000

2 Washington State University
Department of Physics
Shock Dynamics Laboratory
Attn: James R. Asay
Yogendra M. Gupta
Pullman, WA 99164-2814

2 Wright Laboratory
Attn: Dan Brubaker
William Cook
Bruce C. Patterson
Eglin AFB, FL 32542-5434

1 NIMIC, NATO Headquarters
Attn: Peter R. Lee
B-1110 Brussels
BELGIUM

1 M. W. C Dharma-wardana
National Research Council
Ottowa
CANADA K1A 0R6

1 University of British Columbia
Attn: Andrew Ng
Department of Physics & Astronomy
6224 Agricultural Road

Vancouver, BC V6T 1Z1
CANADA

1 Groupe d'Astrophysique (CNRS)
Attn: G. Chabrier
Ecole Normale Supérieure
46 Alée d'Italie
68364 Lyon Cedex 07
FRANCE

2 Commissariat à l'Energie Atomique
Centre d'Etudes de Bruyères-le-Châtel
Attn: Philippe Arnault
Dominique Gilles
BP 12, F91680 Bruyères-le-Châtel
FRANCE

1 Commissariat a l'Energie Atomique
Attn: Jean-Paul Plotard
Coutry, 77181
FRANCE

1 French German Research Institute (ISL)
Attn: Lionel Bourne
5, Rue de General Cassagnon
Saint-Louis Cedex, 68301
FRANCE

1 Institut für Physik
Humbolt-Universität zu Berlin
Attn: Dieter Beule
Invalidenstraße 110
D-10115 Berlin
GERMANY

1 Fachbereich Physik
Universität Rostock
Attn: Ronald Redmer
Universitätsplatz 3
D-18051 Rostock
GERMANY

1 Bhaba Atomic Research Center
High Pressure Physics Division
Attn: S. K. Sikka
Bombay - 400 085
INDIA

1 National Institute for Research
Attn: Toshi Sekine
Inorganic Materials, Namiki 1-1
Tsuhuba, Ibaraki 305-0044
JAPAN

1 Weizmann Institute of Science
Attn: Zeev Zinamon
Rehovot
ISRAEL

1 Yehuda Partom
Rafael, Box 2250
Haifa, 31021
ISRAEL

1 Institute of Chemical Physics
Attn: A. N. Dremin
Russian Academy of Sciences
Moscow, 142432
RUSSIA

2 Institute for High Energy Densities
Russian Academy of Sciences
Attn: V. E. Fortov
I. V. Lomonosov
Izhorskaya ul. 13/19
Moscow, 127412
RUSSIA

1 Russian Federal Nuclear Center
Attn: V. I. Tarzhanov
P.O. Box 245
Snezhinsk, Chelyabinsk 456770
RUSSIA

1 Russian Federal Nuclear Center
Attn: R. F. Trunin
Sarov, Nizhni Novgorod Region 607190
RUSSIA

1 Manfred Held
c/o Messerschmitt-Bölkow-Blohm
GmbH AG
Postfach 1340
Schrobenhausen, 8898
GERMANY

1 M. Musella
European Commission
Joint Research Centre
European Inst. for Transuranium Elements

7615 Karlsruhe
GERMANY

2 AWE
Attn: John Maw
Peter Thompson
Aldermaston, Reading
Berkshire R57 4PR
UNITED KINGDOM

1 MS 0316 J. B. Aidun, 9235
1 0318 P. Yarrington, 9230
1 0751 R. M. Brannon, 6117
1 0819 A. C. Robinson, 9231
1 0819 R. M. Summers, 9231
1 0819 T. G. Trucano, 9211
1 0819 M. K. Wong, 9231
1 0820 P. Chavez, 9232
1 0820 A. V. Farnsworth, 9232
1 0820 M. E. Kipp, 9232
1 0820 S. A. Silling, 9232
1 0820 P. A. Taylor, 9232
1 0834 A. C. Ratzel, 9110
1 0835 E. A. Boucheron, 9141
1 0836 E. S. Hertel, 9116
1 0836 D. Crawford, 9116
1 0836 R. G. Schmidt, 9116
1 0836 M. R. Baer, 9100
1 0836 M. Hobbs, 9116
1 1168 C. Deeney, 1646
1 1168 M. D. Furnish, 1647
1 1178 D. D. Bloomquist, 1630
1 1181 L. C. Chhabildas, 1647
1 1181 J. P. Davis, 1646
1 1181 C. A. Hall, 1647
1 1181 M. Knudson, 1646
1 1181 W. D. Reinhart, 1647
1 1181 T. F. Thornhill, 1647
1 1181 T. J. Vogler, 1647
1 1185 D. P. Kelly, 15417
1 1185 R. J. Dukart, 15417
1 1185 R. J. Weir, 15417
1 1186 M. P. Desjarlais, 1674
1 1186 R. J. Lawrence, 1674
1 1190 J. P. Quintenz, 1600
1 1191 Keith Matzen, 1670
1 1194 D. H. McDaniel, 1640
1 9042 J. J. Dike, 8743
1 9018 Central Technical Files, 8945-1
2 0899 Technical Library,9616